Resonance fluorescence spectrum of a *p*-doped quantum dot coupled to a metallic nanoparticle

F. Carreño, M. A. Antón, and Francisco Arrieta-Yáñez
Facultad de Óptica y Optometría, Universidad Complutense de Madrid, C/ Arcos de Jalón 118, 28037 Madrid, Spain
(Received 29 June 2013; revised manuscript received 1 September 2013; published 8 November 2013)

The resonance fluorescence spectrum (RFS) of a hybrid system consisting of a *p*-doped semiconductor quantum dot (QD) coupled to a metallic nanoparticle (MNP) is analyzed. The quantum dot is described as a four-level atomlike system using the density matrix formalism. The lower levels are Zeeman-split hole spin states and the upper levels correspond to positively charged excitons containing a spin-up, spin-down hole pair and a spin electron. A linearly polarized laser field drives two of the optical transitions of the QD and produces localized surface plasmons in the nanoparticle, which act back upon the QD. The frequencies of these localized plasmons are very different along the two principal axes of the nanoparticle, thus producing an anisotropic modification of the spontaneous emission rates of the allowed optical transitions, which is accompanied by very minor local field corrections. This manifests into dramatic modifications in the RFS of the hybrid system in contrast to the one obtained for the isolated QD. The RFS is analyzed as a function of the nanoparticle's aspect ratio, the external magnetic field applied in the Voigt geometry, and the Rabi frequency of the driving field. It is shown that the spin of the QD is imprinted onto certain sidebands of the RFS, and that the signal at these sidebands can be optimized by engineering the shape of the MNP.

DOI: 10.1103/PhysRevB.88.195303 PACS number(s): 42.50.−p, 78.67.Hc, 78.67.Qa

I. INTRODUCTION

The coherent manipulation of semiconductor quantum dots (QDs) has attracted much interest motivated by the proposal of using QDs as the basic building block of quantum information processing devices, either as single photon emitters[1] or qubits for quantum computers.[2] Their scalability, feasibility of coherent manipulations, strong robustness against relaxation,[3,4] and the flexibility to accommodate their properties (e.g., energy scales) to a specific application, which is not possible for atoms, make them attractive for their integration with the existing technological applications.

In order to reduce decoherence effects, resonant optical excitation in QDs has drawn a lot of attention. As a matter of fact, quantum optical experiments pioneered in atomic vapors in the 1970s have been shown to be achievable in these systems. For example, the resonant excitation of QDs has enabled the observation of Rabi oscillations,[5] the coherent manipulation of excitons,[6] and the observation of Autler-Townes splitting in the optical AC Stark effect. In addition, the Mollow-like absorption spectrum has been demonstrated for a single neutral exciton,[7–9] biexciton[10] and for a single self-assembled charged quantum dot.[11,12] Spin initialization and arbitrary single-qubit rotations for QD's electron spins coupled through a cavity mode while making use of all-optical Raman transitions have been demonstrated as well.[13]

Among other findings, it deserves to be mentioned the collection of resonance fluorescence on a single QD. The embedding of a QD between two distributed Bragg reflectors of moderate reflectivity had allowed the successful recording or the first measurement of RFS in a single self-assembled QD.[8] The use of a moderate-finesse etalon and a dark-field microscope for detection of the RFS have allowed the experimental observation of the Mollow triplet using a single QD. The key advantage of the resonant fluorescence over the spontaneous one is that the resonance fluorescence exhibits much more information about the system under study, including quantum features of interaction of the incident radiation with the system.[14] As an example of this, the application of an external magnetic field in the Faraday geometry allowed for the optical accessing of the QD spin through the analysis of the sidebands in the so-called Mollow quintuplet.[15] The authors pointed out that the spin of the QD is imprinted into the spectrally resolved sidebands of the RFS. The operation in the low driving field regime, the so-called Heitler regime, has allowed us to generate subnatural linewidth and high-coherence quantum light from a single QD.[16] This phenomenon arises from the dominance of the elastic component of the RFS over the incoherent part of the spectrum. These experimental findings open an alternative to produce single photons with laserlike coherence free from any dephasing processes affecting the QD light emission, which is of much interest in quantum information science. This behavior has been also experimentally confirmed in another work,[17] where the fraction of coherently scattered photons was shown to be close to unity for sufficiently weak or detuned pumping of a InAs QD. In these works the self-assembled quantum dot is usually embedded in a high-quality microcavity structure.

In view of the fact that the density of states scales with the ratio of the quality factor of the cavity to the mode volume, the use of small cavities has shown to be a very efficient method to manage the radiative decay rates of a quantum emitter.[18] An alternative to obtain large local photon density of states, accompanied by a significative reduction in the size of the system, is provided by plasmonic systems where light fields are confined to the surface of a MNP. When a quantum emitter is approaching a resonant plasmonic structure, it experiences a strong near-field enhancement as well as a significant modification of the decay rate of its transition channels. The localized surface charge oscillations supported by these particles allow the coupling between the MNP and the quantum emitter, leading to a large resonant enhancement of the local field inside and near the MNP.[19–22] In addition, the local density of states are dramatically altered by the MNP, which results in a modification of the spontaneous

emission rates of the QD's optical transitions.[22–26] Thus, the coupling of a single MNP to a QD can be exploited as a nanoscale cavity[27] offering a route to size reduction with a system size as small as 20 nm^3. The AFM nanomanipulation of the coupling of a single QD to a single gold MNP has been demonstrated experimentally and manifested as a modification of the photoluminescence lifetime from about 30 ns to well below 1 ns.[28] In this experiment the authors reported changes in the photoluminescence of the same QD, thus, eliminating the ambiguity of variable properties of individual QDs. By analogy with photoluminescence, the resonance fluorescence of a QD near the plasmonic nanostructure must also be influenced by the modified incident electromagnetic field and by the modified radiative decay rate of the QD. Very recently, resonance fluorescence assisted by plasmonic structures has been addressed for two level atoms in CW regime[29,30] and under pulsed excitation.[15]

The aim of this work is to extend the investigations in Ref. 30 to study the effects of surface charge oscillations on the RFS of a multilevel hybrid system consisting of a p-doped QD and a spheroidal metallic nanoparticle (MNP) by proper adjustment of the shape of the MNP, the MNP-to-QD distance and the Rabi frequency of the driving field. P-doped QDs are a very promising system to minimize the interaction with the reservoir of QD nuclei spin. The p-type atomistic Bloch function of the hole wave function has a node at the position of the QD nuclei, which in turn results in a dramatic reduction of the hyperfine contact coupling Hamiltonian.[31] Using this approach, Brunner *et al.*[32,33] have experimentally obtained a hole spin relaxation time on the order of 1 ms. Electromagnetically induced transparency (EIT) was also experimentally demonstrated in this system. In particular, we show that the anisotropic enhancement of the QD decay rates arising from the spheroidal geometry of the MNP can modify the resonance fluorescence time scale. This kind of MNP has been shown adequate to accelerate the spin initialization of the QD to a target state.[34] We will consider the so-called Voigt configuration in which the magnetic field is applied along the growth plane of the QD. We present numerical simulations for a representative case of QD, with values of the oscillator strengths, decay rates and the characteristic energy levels taken from experimental studies.[32] It is found that the resonantly excited system exhibits a rich variety of spectral features in the resonance fluorescence of a single QD coupled to the MNP beyond the Mollow triplet found in the two-level case. It is shown that the adjustment of the relative separation between the QD-MNP, the aspect ratio of the MNP and the Rabi frequency of the laser field, the splitting bands and spectral width of molecular fluorescence are dramatically modified. Moreover, with the strong pumping laser, the plasmonic effects can lead to a subnatural narrowing of the spectral lines. In particular, by proper selection of the applied magnetic field and the aspect ratio of the MNP, the spectrally distinguished sideband doublet with information about the spin state is enhanced. These results suggest that the plasmonic effects imprinted in the RFS could serve as a way to spectrally isolate the photons of interest from the original driving field and to obtain information about spin state.

The paper is organized as follows. Section II establishes the model, i.e., the Hamiltonian of the system and the time-evolution equations of the atomic operators assuming the rotating wave approximation. Section III deals with the numerical simulations and explores how the plasmonic interaction influences the RFS of the hybrid system. Finally, Sec. V summarizes the main conclusions.

II. THEORETICAL MODEL

We consider an InAs/GaAs self-assembled QD grown along the Z axis through the Stranski-Krastanov method. The QD is separated by a layer several nanometers thick from a Fermi sea of holes. An applied bias between the top gate and the back contact controls the QD charge state (see Refs. 33 and 35 for specific details). The QD which is charged with a single hole. The ground hole states are labeled $|1_z\rangle \equiv |\Downarrow\rangle$ and $|2_z\rangle \equiv |\Uparrow\rangle$, and the excited trion states are $|3_z\rangle \equiv |\Downarrow\Uparrow\uparrow\rangle$ and $|4_z\rangle \equiv |\Downarrow\Uparrow\downarrow\rangle$. Here $\Uparrow(\Downarrow)$ and $\uparrow(\downarrow)$ denote a heavy hole (HH) and an electron with spins along (against) the Z axis. Hole and electron spin states are naturally degenerate at zero magnetic field, with spin eigenvalues $\pm 1/2$ for electrons and $\pm 3/2$ for holes. The energy level diagram of QD is shown in Fig. 1(a). Selection rules restrict the optically active transition to excitations where the difference in spin between initial and final states is one. Hence, the $|1_z\rangle \leftrightarrow |4_z\rangle$ transition can only be driven by a σ^+ polarized laser field, the transition $|2_z\rangle \leftrightarrow |3_z\rangle$ is restricted to σ^- polarization, and the transitions $|2_z\rangle \leftrightarrow |4_z\rangle$ and $|1_z\rangle \leftrightarrow |3_z\rangle$ remain dark. The application of an external magnetic along the X axis, perpendicular to the sample growth direction, in the so-called Voigt geometry, allows the dark transitions to become bright. The magnetic field introduces an energy shift depending on the carrier spin direction as

$$E_{Zm}^{h(e)} = \tfrac{1}{2}\mu_B(g^{h(e)})B_x. \tag{1}$$

Here, $E_{Zm}^{h(e)}$ is the Zeeman energy shift relative to $B_x = 0$ T, B_x being the magnetic field, and μ_B stands for the Bohr magneton. The quantity $g^{h(e)}$ is the Landé factor of carrier $h(e)$. This magnetic field causes a reference frame transformation from the Z to X basis. The ground hole states are $|1\rangle \equiv |\Downarrow_x\rangle = \frac{1}{\sqrt{2}}(|\Downarrow\rangle - |\Uparrow\rangle)$ and $|2\rangle \equiv |\Uparrow_x\rangle = \frac{1}{\sqrt{2}}(|\Downarrow\rangle + |\Uparrow\rangle)$. In addition, the electron spin states are $|\uparrow_x\rangle = \frac{1}{\sqrt{2}}(|\uparrow\rangle + |\downarrow\rangle)$ and $|\downarrow_x\rangle = \frac{1}{\sqrt{2}}(|\uparrow\rangle - |\downarrow\rangle)$, while the mixed trion states are $|4\rangle = |\Uparrow_x\Downarrow_x\downarrow_x\rangle$, and $|3\rangle = |\Uparrow_x\Downarrow_x\uparrow_x\rangle$. In this new situation each hole spin ground state can be linked to two exciton states via linearly and orthogonally polarized transitions. In particular, the $|1\rangle \leftrightarrow |4\rangle$ and $|2\rangle \leftrightarrow |3\rangle$ transitions become bright with an optical field polarized along the X axis. In addition, $|2\rangle \leftrightarrow |4\rangle$ and $|1\rangle \leftrightarrow |3\rangle$ transitions become allowed with an optical field polarized along the Y axis. The four levels of the system in the Voigt configuration are depicted in Fig. 1(b). Similar arrangements have been previously considered in other works.[36–39] In what follows we consider the scheme depicted in Fig. 1(b) to analyze the RFS of the hybrid system: a linearly, polarized laser E_c along the X axis drives the hole state $|1\rangle$ to an exciton state $|4\rangle$. The system can relax into the desired state $|2\rangle$ or return to state $|1\rangle$, where it can be re-excited by the driving field. Note that the same laser also drives the $|2\rangle \leftrightarrow |3\rangle$ transition, although in a nonresonant way.

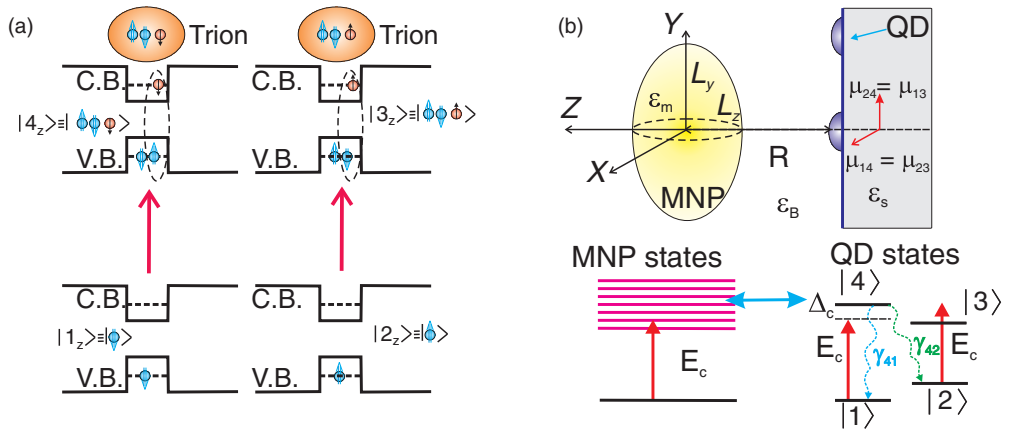

FIG. 1. (Color online) (a) Four level scheme illustrating the ground and excited states of self-assembled QDs. C.B./V.B. stands for the conduction/valence band. (b) Metallic nanospheroid placed close to the QDs. The MNP has a semiminor axis $L_z = L_x$ and semimajor axis L_y and a dielectric constant ϵ_m. The dielectric constants of the QD and the host medium are ϵ_s and ϵ_B, respectively. Atomic states of the positively charged QD and the MNP. The QD atomic states in the X basis are $|1\rangle$ and $|2\rangle$ for the hole spin eigenvectors, split by the Zeeman effect; and the upper levels $|3\rangle$ and $|4\rangle$ are X^{1+} excitons consisting of two spin-paired holes in the V.B. and an unpaired electron with spin $\pm 1/2$ in the C.B. The straight lines indicate the driving field linearly polarized along the X axis. The wavy lines indicate the spontaneous relaxations from the upper level $|4\rangle$ to the ground states. In addition, γ_{32} and γ_{31} are the decay rate of the upper level $|3\rangle$ to the ground states transitions (not shown).

The narrowing/broadening of a line shape is associated to a decrease/increase of its associated decay rate. Here we are interested in the obtention of subnatural linewidths. Thus, in order to lengthen the characteristic time to transfer the population to the target state $|2\rangle$, we pursue to selectively decelerate the decay rate from the trion state $|4\rangle$ to the target state $|2\rangle$, while keeping the other decay rate transition $|4\rangle \leftrightarrow |1\rangle$ nearly unchanged. To accomplish this a MNP with nanospheroid geometry is placed close to the QD as shown in Fig. 1(b). The center-to-center distance between the QD and the MNP is denoted as R. The semiminor axis and semimajor axis of the MNP are $L_x = L_z$ and L_y, respectively [Fig. 1(b)]. We define the aspect ratio of the nanospheroid as $q = L_y/L_z$. We will show that the appropriate engineering of the shape of the MNP will result in a way to tailor the dynamics of the QD-MNP hybrid system, which in turn should manifest as dramatic modifications in the RFS of the system. The driving field E_c is assumed to be spatially uniform over the relatively small dimensions of the hybrid system, and this allows us the use of the quasistatic approximation[40] when describing the interaction of the light field with the MNP. The dielectric function of the QD is ϵ_s, while that of the host medium is labeled as ϵ_B [see Fig. 1(b)]. The dielectric function of the MNP, $\epsilon_m(\omega)$, is taken in a renormalized Drude approximation as

$$\epsilon_m(\omega) = \epsilon_\infty - \frac{\omega_p^2}{\omega^2 + i\gamma_p\omega}, \tag{2}$$

ϵ_∞ being the high-frequency limit of the metal dielectric function, ω_p stands for the bulk plasma frequency, and γ_p is the Landau damping constant.

The system is driven by a classical light field with amplitude E_c and angular frequency ω_L, which is assumed to be linearly polarized in the X direction and reads as

$$\vec{\mathcal{E}}_c = \tfrac{1}{2}\hat{u}_x E_c(t) e^{-i\omega_L t} + \text{c.c.}, \tag{3}$$

$\hat{u}_x$ being the unitary vector along the X axis. Therefore, the driving field only couples transitions $|1\rangle \leftrightarrow |4\rangle$ and $|2\rangle \leftrightarrow |3\rangle$.

The time evolution of the density matrix reads

$$\frac{\partial\rho}{\partial t} = -\frac{i}{\hbar}[H,\rho] - \mathcal{L}\rho, \tag{4}$$

where H is the Hamiltonian of the hybrid system and is explicitly given by

$$H = \hbar\sum_{j=1}^{4}\omega_j\sigma_{jj} - \frac{1}{2}\left[\mu_{41}\sigma_{41} + \mu_{32}\sigma_{32}\right]E_{QD}^{(x)}e^{-i\omega_L t} + \text{H.c.}. \tag{5}$$

In the above expression, $\sigma_{ij} = |i\rangle\langle j|$ are the excitonic operators and μ_{ij} is the dipole moment of the transition $|i\rangle \leftrightarrow |j\rangle$. The quantity $E_{QD}^{(x)}$ represents the slowly varying amplitude of the total field felt by the QD, which drives the $|1\rangle \leftrightarrow |4\rangle$ and $|2\rangle \leftrightarrow |3\rangle$ transitions. This field is nothing but the sum of the driving field and the field due to the polarization of the MNP arising from the charge induced on its surface by the field due to the QD (see Appendix A for a summary of the derivation and Ref. 34 for full details). A straightforward calculation allows to establish the relationship between these fields and allows to rewrite the total Hamiltonian of the QD in the dipole approximation as follows

$$H = \hbar\sum_{j=1}^{4}\omega_j\sigma_{jj} - \hbar\left[\Omega_c + G_c\left(\rho_{41} + \rho_{32}\right)\right] \times \left(\sigma_{41} + \sigma_{32}\right)e^{-i\omega_L t} + \text{H.c.}, \tag{6}$$

where we have introduced the magnitudes Ω_c and G_c, which account for the effects of both the driving field and the

plasmonic interaction, and are explicitly given by

$$\Omega_c^0 = \frac{\mu_{41} E_c}{2\hbar\epsilon_{\text{effs}}},$$
$$\Omega_c = \Omega_c^0 \left[1 + \frac{S_x q L_x^3 \gamma_x(\omega_L)}{R^3}\right], \tag{7}$$
$$G_c = \frac{S_x^2 \mu_{41}^2 q L_x^3 \gamma_x(\omega_L)}{8\pi\epsilon_0 \epsilon_B \hbar \epsilon_{\text{effs}} R^6},$$

where we have assumed that $\mu_{41} = \mu_{32}$. In the above equations, Ω_c is the renormalized Rabi frequency associated with the driving field and the field produced by the induced dipole moment $P_{\text{MNP}}^{(x)}$ of the MNP. Note that G_c is a complex quantity whose imaginary part represents the Förster energy transfer rate from the QD to the MNP, while its real part accounts for the red shift of the QD transition caused by the plasmonic interaction.[20,41]

Finally the term $\mathcal{L}\rho$ in Eq. (4) accounts for the spontaneous decay rates of the involved transitions, which are described by Lindblad terms

$$\begin{aligned}\mathcal{L}\rho = &\frac{\gamma_{41}^p}{2}(\rho\sigma_{44} + \sigma_{44}\rho - 2\sigma_{14}\rho\sigma_{41}) \\ &+ \frac{\gamma_{42}^p}{2}(\rho\sigma_{44} + \sigma_{44}\rho - 2\sigma_{24}\rho\sigma_{42}) \\ &+ \frac{\gamma_{31}^p}{2}(\rho\sigma_{33} + \sigma_{33}\rho - 2\sigma_{13}\rho\sigma_{31}) \\ &+ \frac{\gamma_{32}^p}{2}(\rho\sigma_{33} + \sigma_{33}\rho - 2\sigma_{23}\rho\sigma_{32}) \\ &+ \frac{\gamma_{21}}{2}(\rho\sigma_{22} + \sigma_{22}\rho - 2\sigma_{12}\rho\sigma_{21}).\end{aligned} \tag{8}$$

Here, γ_{ij}^p with $i = 3,4$ and $j = 1,2$ stand for the spontaneous emission decay rates of the QD. These parameters are modified by the plasmonic field of the MNP. The dissipative process described by the term of the Liouvillian with the prefactor γ_{21} accounts for the lower levels' dephasing and is assumed to be uncoupled with the localized surface plasmons due to the low values of the Zeeman splitting considered.

Following previous works[26,42] we can derive the new spontaneous decay rates in terms of their free-space values, by resorting to a classical calculation in the quasistatic limit in which the QD is treated as a point dipole. The radiative decay rate of the atomic transitions modified by the coherent-plasmonic field enhancement are given by

$$\begin{aligned}\gamma_{41}^p = \gamma_{32}^p = \gamma_{41}^{(0)} F_{enh}^x, \\ \gamma_{42}^p = \gamma_{31}^p = \gamma_{42}^{(0)} F_{enh}^y,\end{aligned} \tag{9}$$

where the superindex 0 is used to indicate the values of the decay rates in free space. The enhancement factors read as

$$F_{enh}^x = \left|1 + \frac{S_x q L_x^3 \gamma_x(\omega_L)}{R^3}\right|^2, \tag{10}$$

$$F_{enh}^y = \left|1 + \frac{S_y q L_x^3 \gamma_y(\omega_L)}{R^3}\right|^2. \tag{11}$$

We refer the reader to Ref. 34 for more details. A similar approach to estimate the modification of the decay rates has been used in other works (see for example Refs. 30,43–47). It is worth noting that depending on the orientation of the dipole moments of the QD emitter's transitions, the decay rates could become very different from one another, i.e., the value of F_{enh}^y can strongly differ from that of F_{enh}^x. This will result in an anisotropic Purcell factor enhancement which will have important consequences for controlling the time dynamics of this nanohybrid system, and can lead to the anisotropic acceleration or deceleration of the decay rates.

From Eq. (6) and Eq. (8), we obtain the following equations of motion for the density matrix elements of the QD in the hybrid system:

$$\begin{aligned}
\frac{\partial\rho_{41}}{\partial t} &= -[\Gamma_{41} - i\Delta_c]\rho_{41} + i[\Omega_c + G_c(\rho_{41} + \rho_{32})]\rho_{21} + i[\Omega_c + G_c(\rho_{41} + \rho_{32})](\rho_{11} - \rho_{44}), \\
\frac{\partial\rho_{31}}{\partial t} &= -[\Gamma_{31} - i(\Delta_c + 2\Delta_e)]\rho_{31} + i[\Omega_c + G_c(\rho_{41} + \rho_{32})]\rho_{21} - i[\Omega_c + G_c(\rho_{41} + \rho_{32})]\rho_{34}, \\
\frac{\partial\rho_{21}}{\partial t} &= -[\Gamma_{21} + i\omega_{21}]\rho_{21} + i[\Omega_c^* + G_c^*(\rho_{14} + \rho_{23})]\rho_{31} - i[\Omega_c + G_c(\rho_{41} + \rho_{32})]\rho_{24}, \\
\frac{\partial\rho_{43}}{\partial t} &= -[\Gamma_{43} + i2\Delta_c]\rho_{43} + i[\Omega_c + G_c(\rho_{41} + \rho_{32})]\rho_{13} - i[\Omega_c^* + G_c^*(\rho_{14} + \rho_{23})]\rho_{42}, \\
\frac{\partial\rho_{42}}{\partial t} &= -[\Gamma_{42} - i(\Delta_c + 2\Delta_g)]\rho_{42} + i[\Omega_c + G_c(\rho_{41} + \rho_{32})]\rho_{12} - i[\Omega_c + G_c(\rho_{41} + \rho_{32})]\rho_{43}, \\
\frac{\partial\rho_{32}}{\partial t} &= -[\Gamma_{32} - i(\Delta_c + 2\Delta_e + 2\Delta_g)]\rho_{32} + i[\Omega_c + G_c(\rho_{41} + \rho_{32})](\rho_{22} - \rho_{33}), \\
\frac{\partial\rho_{44}}{\partial t} &= -\left(\gamma_{41}^p + \gamma_{42}^p\right)\rho_{44} + i[\Omega_c + G_c(\rho_{41} + \rho_{32})]\rho_{14} - i[\Omega_c^* + G_c^*(\rho_{14} + \rho_{23})]\rho_{41}, \\
\frac{\partial\rho_{33}}{\partial t} &= -\left(\gamma_{31}^p + \gamma_{32}^p\right)\rho_{33} + i[\Omega_c + G_c(\rho_{41} + \rho_{32})]\rho_{23} - i[\Omega_c^* + G_c^*(\rho_{14} + \rho_{23})]\rho_{32}, \\
\frac{\partial\rho_{22}}{\partial t} &= -\gamma_{21}\rho_{22} + \gamma_{32}^p\rho_{33} + \gamma_{42}^p\rho_{44} + i[\Omega_c^* + G_c^*(\rho_{14} + \rho_{23})]\rho_{32} - i[\Omega_c + G_c(\rho_{41} + \rho_{32})]\rho_{23}.
\end{aligned} \tag{12}$$

We assume the following definitions of the dephasing rates: $\Gamma_{41} = (\gamma_{41}^p + \gamma_{42}^p)/2$, $\Gamma_{21} = \gamma_{21}/2$, $\Gamma_{32} = (\gamma_{31}^p + \gamma_{32}^p + \gamma_{21})/2 = \Gamma_{41} + \Gamma_{21}$. $2\Delta_e = E_{Zm}^e$, and $2\Delta_g = E_{Zm}^h$. Finally, $\Delta_c = \omega_{41} - \omega_L$ denotes the optical detuning of the driving field. The population of the ground level ρ_{11} is computed considering a closed system, i.e., $\rho_{11} = 1 - \rho_{22} - \rho_{33} - \rho_{44}$.

A close inspection of Eq. (12) reveals that the plasmonic interaction manifests in three different ways: The first relies on the plasmon-induced modification of the spontaneous decay rates. The second is related with the enhancement of the Rabi frequency, which drives the QD according to the expression given in Eq. (7). The third manifestation of the plasmonic interaction can be formally interpreted as a nonlinear frequency shift in the optical resonance, causing a dynamical detuning and a nonradiative decay rate. For example, in the case of the optical coherence ρ_{41}, the dynamical detuning is given by $\mathrm{Re}(G_c)(\rho_{11} - \rho_{44})$, whereas the dynamical decay rate (nonradiative decay rate) is given by $\mathrm{Im}(G_c)(\rho_{11} - \rho_{44})$. The above mentioned mechanisms strongly depend on the QD-MNP distance R. The last two mechanisms have been explored in the context of selective excitonic population in a QD-MNP hybrid system,[48] and in the case of considering how to obtain an accelerated hole spin initialization.[34]

A. Fluorescence spectra of the hybrid system

We proceed to analyze how the MNP affect to the RFS of the QD-MNP hybrid system. This spectrum is proportional to the Fourier transformation of the steady-state correlation function $\lim_{t\to\infty}\langle E^-(r,t'+t)\cdot E^+(r,t)\rangle$, where $E^-(r,t)/E^+(r,t)$ is the negative/positive frequency part of the radiation field in the far zone. The radiation field consists of a free-field operator and a source-field operator that is proportional to the atomic polarization operator.[49] Therefore, the RFS can be expressed in terms of the atomic correlation function

$$S(\omega) = \Re\left[\int_0^\infty \lim_{t\to\infty}\langle D^+(t'+t)\cdot D^-(t)\rangle e^{-i\omega t'}dt'\right], \quad (13)$$

where $\Re[\,]$ denotes the real part of the magnitude enclosed in square brackets, and $D^+(t)$ is the atomic polarization operator

$$D^+(t) = \vec{\mu}_{14}\sigma_{41}(t) + \vec{\mu}_{13}\sigma_{31}(t) + \vec{\mu}_{24}\sigma_{42}(t) + \vec{\mu}_{23}\sigma_{32}(t). \quad (14)$$

and $D^-(t) = [D^+(t)]^\dagger$.

In writing Eq. (13) and in the rest of this section, we abbreviate $\omega - \omega_L$ by ω, but we should interpret ω as a frequency measured relative to the laser frequency ω_L. We are only interested in the incoherent part of the RFS, which is given by

$$S_{\mathrm{inc}}(\omega) = \Re\left[\int_0^\infty \lim_{t\to\infty}\langle \Delta D^+(t'+t)\cdot \Delta D^-(t)\rangle e^{-i\omega t'}dt'\right], \quad (15)$$

where $\Delta D^\pm(t') = D^\pm(t') - \langle D^\pm(\infty)\rangle$ stands for the deviation of the dipole polarization operator from its mean steady-state value. The calculation of $S_{\mathrm{inc}}(\omega)$ requires the calculation of the two-time correlation function, which can be performed by means of the quantum-regression theorem[49,50] (see Appendix B for details).

In Sec. III we will present the results of the RFS of the hybrid system by means of numerical simulations, and we will discuss the role of the previously mentioned mechanisms by making use of the so-called dressed state picture.

III. RESULTS AND DISCUSSION

We consider the data for the QD reported in Ref. 32. In particular, the radiative decay rates of the transitions are $\hbar\gamma_{41}^{(0)} = \hbar\gamma_{42}^{(0)} = \hbar\gamma_{32}^{(0)} = \hbar\gamma_{31}^{(0)} \equiv \hbar\gamma_0 = 0.5\ \mu$eV, the hole spin decay rate is $\gamma_{21} \simeq 0.000671\ \mu$eV, and the ground-level Zeeman splitting is $2\hbar\Delta_g = 18\ \mu$eV. These data correspond[32] to a temperature of 4.2 K and a magnetic field of 2.3 T. We assume an upper value for the Zeeman splitting $2\hbar\Delta_e \simeq 10\ \mu$eV. We also consider the driving field resonant with transition $|1\rangle \leftrightarrow |4\rangle$, i.e., $\Delta_c = 0$ ($\lambda \simeq 947$ nm). In addition, the dielectric constant of the QD is taken as $\epsilon_s = 12.96$, and the dielectric constant of the host material is set to $\epsilon_B = 2.25$. The MNP is a gold nanospheroid with semiminor axis $L_x = L_z = 8$ nm, and its semimajor axis L_y is scaled with the aspect ratio $q = L_y/L_z$. The plasma frequency is set to $\hbar\omega_p = 8.56$ eV, the high-frequency limit $\epsilon_\infty = 9.54$, and the damping constant $\hbar\gamma_p = 0.066$ eV. With these parameters, the Drude model assumed in Eq. (2) provides a reasonably good fit to tabulated experimental data for photon energies smaller than 3 eV.[51]

As a first step in our study we focus our attention on the modifications of the spontaneous emission rates due to the presence of the MNP. Figures 2(a)–2(b) show the radiative decay rates γ_{42}^p and γ_{41}^p modified by the presence of the MNP as a function of the aspect ratio q for several distances R from the QD center to the MNP center. A close inspection of these figures shows a highly distinctive behavior for the two decay rates: The γ_{41}^p decay rate shows a monotonous and smooth decrease versus the aspect ratio for all the distances considered, whereas the γ_{42}^p decay rate presents a dispersivelike behavior with a large variation in comparison to the value achieved in free space. In fact, γ_{42}^p presents a variation for a certain range of q's where the decay rate is diminished in comparison to that achieved in free space, and more interestingly, another interval for q where this decay rate is strongly enhanced up to a factor close to 10^2 times the value in free space. In particular, there exists a certain value of the aspect ratio around $q \simeq 4.6$ for which the enhancement is maximized. This anisotropic behavior is associated with the difference between the longitudinal surface plasmon resonance along the Y axis and the transverse surface plasmon resonance along the X axis. This resonant behavior can be showed up by computing the angular frequencies of the localized surface plasmon polaritons (SPPs) labeled as $\omega_{\mathrm{spy(x)}}$ along the principal axes $Y(X)$, which read as

$$\omega_{\mathrm{spj}} = \sqrt{\frac{\varsigma_j}{\epsilon_B + \varsigma_j(\epsilon_\infty - \epsilon_B)}}, \quad j = y,x. \quad (16)$$

These frequencies are determined by setting to zero the real part part of the denominator of $\gamma_y(\omega_L)$ and $\gamma_x(\omega_L)$, and solving for ω (see also Ref. 42). Let us consider for example the case with $q = 4.6$ and a distance $R = 40$ nm. The values obtained are $\omega_{\mathrm{spy}} = 1.3016$ (eV) and $\omega_{\mathrm{spx}} = 2.4618$ (eV), whereas the atomic transition frequency is $\omega_{41} = 1.3116$ (eV). This

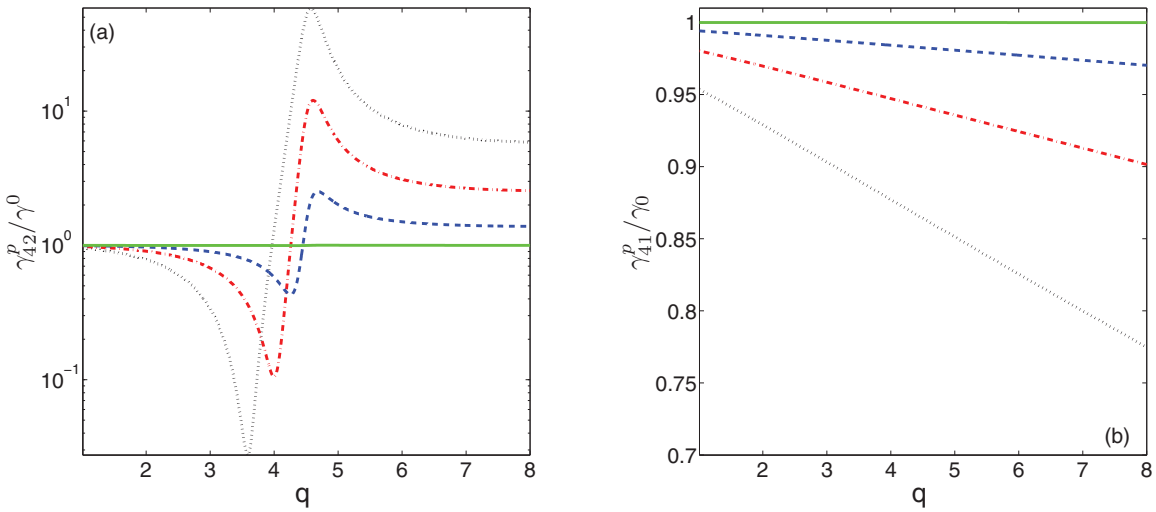

FIG. 2. (Color online) (a), (b) Plasmon-modified radiative decay rates of the QD $\gamma_{42}^p \backslash \gamma_{41}^p$ normalized to γ_0 versus the aspect ratio (q) of the MNP for several distances R from the QD to the MNP: $R = 30$ nm (dotted line), $R = 40$ nm (dashed-dotted line), $R = 60$ nm (dashed line), and $R = 400$ nm (solid line).

numerical example illustrates that a proper selection of the shape factor of the MNP allows for the excitation of the SPPs along the Y axis, whereas those along the X axis remain almost unexcited.

In order to get some further insight into the behavior of the curves depicted in Fig. 2(a), we resort to approximate magnitude F_{enh}^y in the case that the angular frequency of the driving field is on resonance with the atomic transition frequency ($\omega_L \approx \omega_{41}$). Thus we can approximate γ_y to

$$\gamma_y \approx -\frac{\omega_{\rm spy}^2}{6\varsigma_y \omega_L} \frac{\omega_L - \omega_{\rm spy}}{(\omega_L - \omega_{\rm spy})^2 + (\gamma_p/2)^2}, \tag{17}$$

and the coherent-plasmonic enhancement factor F_{enh}^y can be simplified to

$$F_{enh}^y \approx \left| 1 + q \left(\frac{L_x}{R} \right)^3 \frac{\omega_{\rm spy}^2}{6\varsigma_y \omega_{41}} \frac{\omega_{41} - \omega_{\rm spy}}{(\omega_{41} - \omega_{\rm spy})^2 + (\gamma_p/2)^2} \right|^2, \tag{18}$$

In the case with $q \in [1, 4.6]$ the surface plasmon frequency along the Y axis is larger than the atomic transition frequency ($\omega_{\rm spy} > \omega_{41}$), thus the second term of the right-hand side of the Eq. (18) takes a negative value, and therefore magnitude F_{enh}^y is less than unity, i.e., the spontaneous emission rate is significantly inhibited, in accordance with the behavior of an emitter inside a cavity.[30,52,53] On the other hand, in the case where $\omega_{\rm spy} < \omega_{41}$, which holds in the interval $q \in [4.6, 8]$, this term becomes positive, resulting in an enhancement of the spontaneous emission rate ($F_{enh}^y > 1$). A similar behavior has been found in Refs. 54 and 55. Thus, the MNP acts as a nanoscale cavity which decreases (enhances) the strength of the vacuum fluctuations depending $\omega_{\rm spy}$ lies above (below) the atomic transition frequency ω_{41}. In summary, all these facts indicate that the engineering of the shape and the size of the nanospheroid can be used to enhance on demand the spontaneous emission in a selected atomic transition of the QD. This anisotropic resonant phenomenon is the key idea that allows the selective plasmonic acceleration of the decay of the transition $|2\rangle \leftrightarrow |4\rangle$ in comparison with the almost unaltered transition $|1\rangle \leftrightarrow |4\rangle$.[34] We will show that this will result in dramatic modifications in the RFS of the hybrid system.

The anisotropic enhancement of the decay rates of the atomic transitions is accompanied by the simultaneous modification of the nonlinear parameter G_c defined in Eq. (7). The terms involving G_c in Eq. (12) accounts for the local-field corrections arising from plasmon interaction that takes place due to the proximity between the QD and the MNP. The influence of such local-field corrections has been previously addressed in other hybrid systems (see Ref. 48) in the context of obtaining selective population transfer in a time regime where the effects of the enhancement of the decay rates remained negligible, and in the case of considering spin hole initialization (see Ref. 34). Here we are interested in analyzing how the RFS is modified by the presence of the MNP. Note that the calculation of the RFS relies on the use of the quantum regression theorem (see Appendix B), which in turn makes use of the fact that the equation of motion of the system remain in the linear regime. Thus we should check whether the nonlinear effects in Eq. (12) remain negligible or not.

Let us start by comparing how the MNP modifies the RFS of the QD. To this end, we have selected the distance $R = 40$ nm, whereas the aspect ratio of the MNP is set to $q = 4$, which results in $\gamma_{42}^p \approx 0.105\gamma_0$ [very close to the minimum of the dashed-dotted line in Fig. 2(a)] and $\gamma_{41}^p \approx 0.947\gamma_0$. This choice results in $\mathrm{Re}(G_c) \approx 0.019\gamma_0$, and $\mathrm{Im}(G_c) \approx 0.0002\gamma_0$, so that the terms involving G_c in Eq. (12) do not play a significant role in the time dynamics of the system, i.e., the nonlinear terms in Eq. (12) can be neglected and we deal with a linear problem. In other words, these data indicate that the asymmetric enhancement of the decay rates is significative, while the local field effects remain negligible. Figure 3(a) presents the RFS of the QD in the absence of the MNP (dashed line) in the case that the Rabi frequency of the driving field is set to $\Omega_c^0 = 1.5\gamma_0$. The central line exhibits only one single peak. In addition, we can devise the appearance of two weak blue sidebands

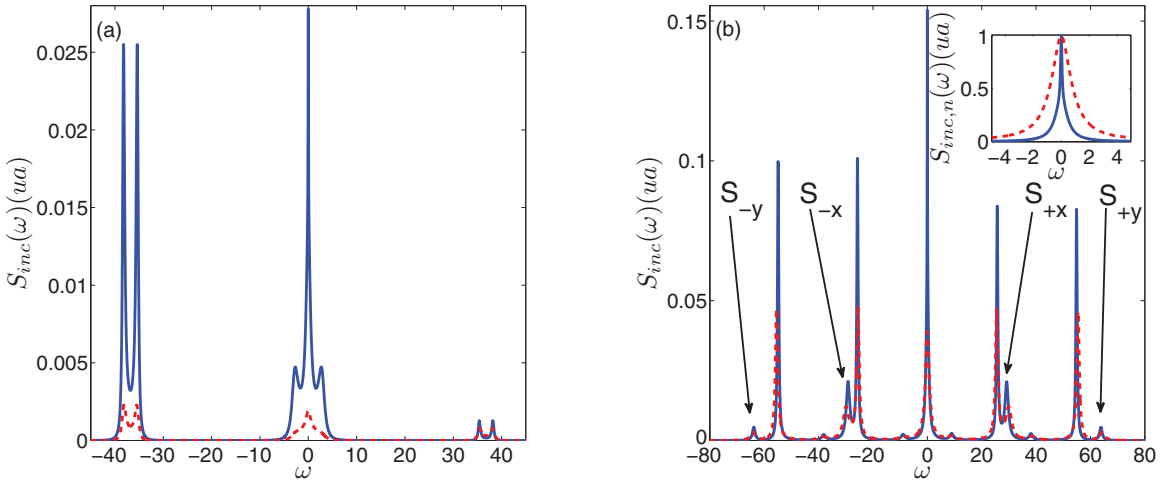

FIG. 3. (Color online) $S_{\rm inc}(\omega)$ versus ω for the isolated QD (dashed line) and the hybrid system (solid line) with $R = 40$ nm. (a) $\Omega_c^0 = 1.5\gamma_0$ and (b) $\Omega_c^0 = 15\gamma_0$. The aspect ratio is $q = 4$ and the magnetic field is set to $B_x = 2.3$ T. The inset displays the normalized central line.

and two additional red sidebands. The latter being slightly greater than the former. Under similar illumination conditions, the presence of the gold nanoparticle splits the central line into a Mollow-like structure (solid line), and the peak values of the blue and red sidebands become strongly enhanced. Furthermore, the central line displays a subnatural linewidth.

An increase of the Rabi frequency ($\Omega_c^0 = 15\gamma_0$), results in a full development of the RFS into all the possible optical transitions (up to 13 peaks can be observed) consisting in six blue/red sidebands and the central line as displayed in Fig. 3(b). This result should not come as a surprise, since at such a high pump value of the driving field, even the detuned state |3> experiences a non-negligible population, which in turn contributes to produce spontaneous photons, which manifest as the emergence of the tiny transitions. It is worth mentioning that a Mollow-like quintuplet has been experimentally observed in the case of analyzing the RFS of InAs/GaAs quantum dots with a weak external field of 120 mT applied in the Faraday geometry (see Ref. 15 for details). The inset in Fig. 3(b) shows the normalized RFS around the central line in the absence (presence) of the MNP [dashed (solid line)], revealing the narrowing of such line due to the plasmonic interaction. In a free-space situation, the use of such high values of the driving field will lead to the development of the sidebands and each one of them will become power broadened. We have shown in Fig. 2 that the presence of the MNP alters the local density of states, which in turn manifests as a decrease in the decay rates. These two competing mechanisms result in a global reduction of the linewidths, indicating us that the plasmonic interaction dominates over the power broadening. It is to be noted that measuring the spectral separation of the largest red sideband from the blue sideband it is possible to achieve photon emission across a frequency band of ∼84 GHz. This is nearly 110 times larger than the 0.76 GHz spontaneous emission rate. This is by no mean an upper limit, but can be further increased by laser detuning, i.e., by setting $\Delta_c \neq 0$.

We will show later in this work that the inner sidebands $S_{\pm x}$ and the outermost sidebands $S_{\pm y}$ [see Fig. 3(b)] correspond to optical transitions between dressed states $\alpha\rangle \leftrightarrow |\beta\rangle$ and $\gamma\rangle \leftrightarrow |\delta\rangle$, respectively. These transitions only involve the generation of flying photons which preserve the spin information. We note that the emission of such photons from these two sidebands is anticorrelated, determined by the hole spin. Therefore, by filtering the RFS to a spin sideband, quantum dot spin measurement with above-unity signal-to-noise ratio can be carried out. A similar behavior has been observed in the case of an isolated n-doped QD.[15]

In the following we will see that the narrowing of the central line previously found in Fig. 3(b) together with the emergence of the sidebands $S_{\pm x}$ and $S_{\pm y}$, which allow for the access to the QD spin, can be further engineered by a proper selection of the distance R and the aspect ratio q. To this end, we have computed the modified decay rate γ_{42}^p for distances R ranging from 20–200 nm. For each one of the distances considered, we also allowed the aspect ratio to vary within the interval $q \in [1, 10]$, and the aspect ratio at which such decay rate reaches its minimum value ($q_{\rm min}$) was selected. The results are displayed in Fig. 4(a). Note that in the case of small distances between the QD and the MNP ($R < 50$ nm), the anisotropy of the decay rates becomes large. However for larger distances the anisotropy decreases and the decay rates approach to the free-space decay rate γ_0. This behavior allows us to select the aspect ratio $q_{\rm min}$, which optimizes the Purcell anisotropy and the signal of the sidebands of interest in the RFS. Figure 4(b) shows the RFS obtained for two different pair of values ($R = 20$ nm, $q_{\rm min} = 2.726$) (solid line) and ($R = 40$ nm, $q_{\rm min} = 4$) (dashed line), and the same value of the Rabi frequency $\Omega_c^0 = 14\gamma_0$. The outermost sidebands $S_{\pm y}$ remain with reduced peak values in this situation. More interestingly, the sidebands $S_{\pm x}$ are not resolved for the largest distance (see the dashed line in the right and left insets with vertical linear scale). This behavior contrasts with the one displayed in Fig. 3(b), which was obtained for a slightly greater value of the Rabi frequency ($\Omega_c^0 = 15\gamma_0$). The situation is dramatically modified when changing the distance to $R = 20$ nm and the aspect ratio to $q = 2.726$: in this case the sidebands $S_{\pm x}$ with solid line are clearly resolved from their adjacent sidebands. It should be remarked that the red-shifted

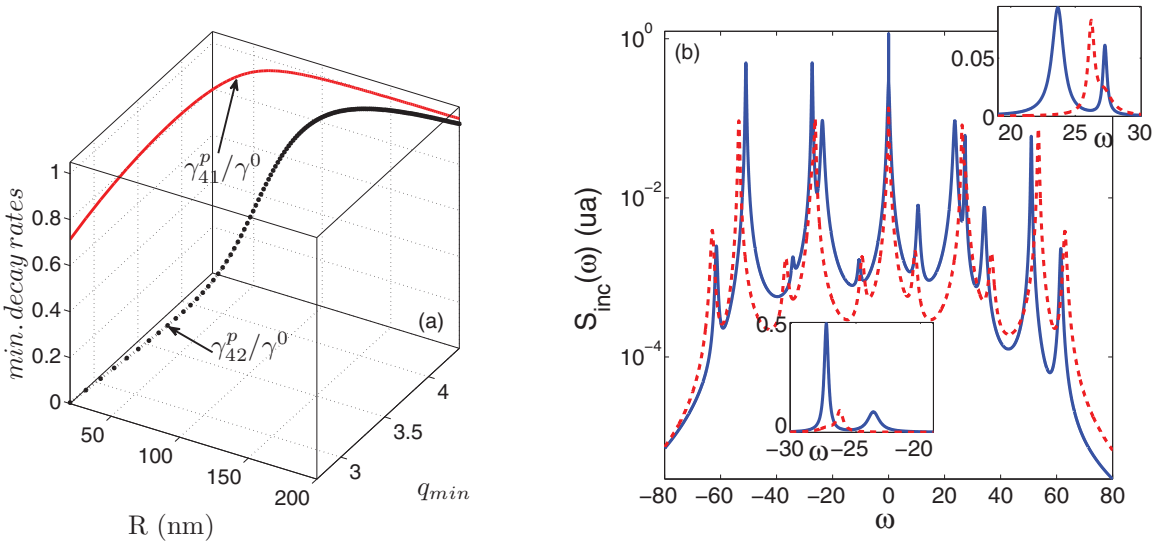

FIG. 4. (Color online) (a) Modified decay rates γ^p_{41} and γ^p_{42} normalized to γ_0 as a function of the distance R and the aspect ratio $q_{\min}$. For each R value, the aspect ratio $q_{\min}$ is the one at which the decay rate γ^p_{42} reach its minimum value. (b) $S_{\rm inc}(\omega)$ versus ω of the hybrid system for the pair of values (R,$q_{\min}$): (20 nm, 2.726) (solid line) and (40 nm, 4) (dashed line). The Rabi frequency of the driving field is $\Omega^0_c = 14\gamma_0$, and the magnetic field is set to $B_x = 2.3$ T.

sideband S_{-x} experiences a huge enhancement in comparison to the signal obtained at the twin sideband S_{+x}. In addition, the sideband S_{-x} exhibits a twentyfold enhancement with regard to the signal achieved in the conditions of solid line in Fig. 3(b).

Up to now we have considered a situation where the driving field is on resonance with transition $|1\rangle \leftrightarrow |4\rangle$, i.e., $\Delta_c = 0$. In such situation, the asymmetries found in the RFS arise from the fact that the Zeeman-split upper levels $|3\rangle$ and $|4\rangle$ are pumped in an asymmetric way while the initial population is in level $|1\rangle$. One may expect that the use of a detuned driving field will reinforce the asymmetry of the system and it will bring a new parameter to tune on demand the spectral features of the RFS. Figure 5 presents the spectra obtained for two non-null values of the detuning Δ_c while keeping the rest of parameters as those used to produce the curve in solid line in Fig. 4(b). In Fig. 5 we can appreciate that the use of a negative value for Δ_c results in an way to make transition $|2\rangle \leftrightarrow |3\rangle$ more effective: the essence of this effect lies in the imbalance of the effective Rabi frequency ($\Omega_{\rm eff} = \sqrt{\Delta_c^2 + \Omega_c^2}$) experienced by the two pumped bare transitions. Here, we use the Δ_c dependence to enforce such imbalance and enables to imprint the spin information onto the sidebands $S_{\pm x/y}$: for a negative value of Δ_c (solid line) the sidebands $S_{\pm x}$ are not spectrally resolved (see the inset at the bottom of the figure) while the outermost sidebands $S_{\pm y}$ remain resolved and they exhibit weak peak values. However, the use of a positive value for Δ_c (dashed line) allows to resolve the $S_{\pm x}$ from their corresponding nearest sidebands.

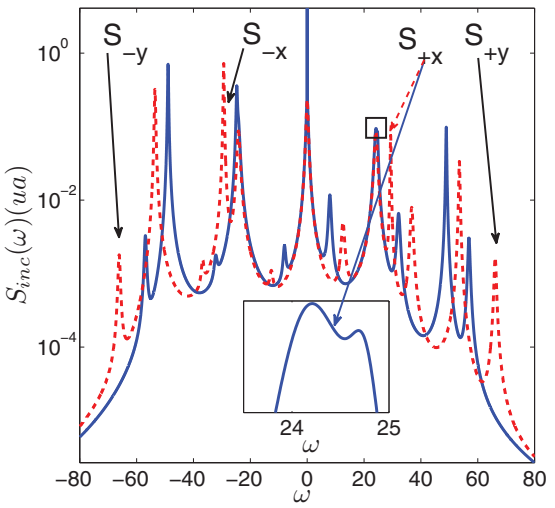

FIG. 5. (Color online) $S_{\rm inc}(\omega)$ versus ω for the QD-MNP hybrid system in the case with $R = 20$ nm, $q = 2.726$, the Rabi frequency of the driving field is $\Omega^0_c = 14\gamma_0$, and the magnetic field is set to $B_x = 2.3$ T. The detuning of the driving field is set to $\Delta_c = -5\gamma_0$ (solid line) and $\Delta_c = +5\gamma_0$ (dashed line).

IV. ANALYSIS OF RFS IN THE DRESSED-STATE PICTURE

In this section we derive analytic expressions for the line shapes and linewidths of the RFS in the dressed state basis in order to explain the main features of the spectra previously obtained. The dressed states are found by looking for the eigenvalues (λ_k ,$k = \alpha,\beta,\delta,\gamma$) and eigenvectors ($|k\rangle$,$k = \alpha,\beta,\delta,\gamma$) of the atomic plus coherent part of the Hamiltonian in Eq. (6) in the rotating frame:

$$H^{rf} = 2\hbar\Delta_g\sigma_{22} - \hbar(\Delta_c + 2\Delta_e)\sigma_{33} - \hbar\Delta_c\sigma_{44} - \hbar\Omega_c^*\sigma_{14} - \hbar\Omega_c^*\sigma_{23} - \hbar\Omega_c\sigma_{32} - \hbar\Omega_c\sigma_{41}. \quad (19)$$

By assuming that the driving field is resonant with the bare atomic transition ($\Delta_c = 0$), the eigenvalues are found to be given by:

$$\lambda_\alpha = +\hbar|\Omega_c|, \quad \lambda_\beta = -\hbar|\Omega_c|, \quad \lambda_\delta = \hbar(\overline{\Delta} + \Omega_R), \quad \lambda_\gamma = \hbar(\overline{\Delta} - \Omega_R), \quad (20)$$

where $\overline{\Delta} = \Delta_g - \Delta_e$, and $\Omega_R = \sqrt{(\Delta_g + \Delta_e)^2 + |\Omega_c|^2}$. The eigenvectors [solutions to the equation $(H - \lambda_k\hat{I})|k\rangle = 0$, $\hat{I}$

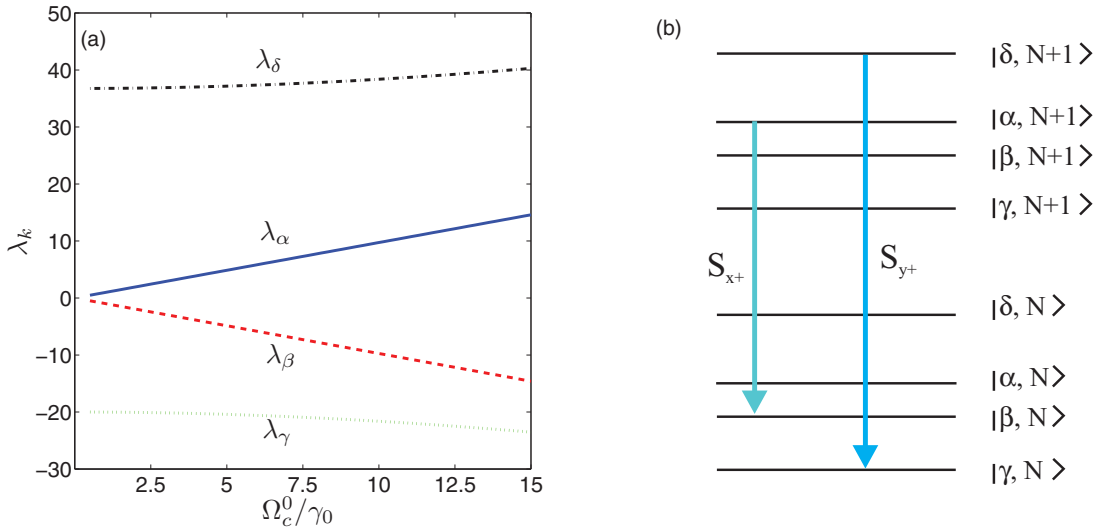

FIG. 6. (Color online) (a) Eigenvalues of the Hamiltonian versus the Rabi frequency of the driving field Ω_c^0. (b) Transition frequencies between adjacent manifolds of dressed states, indicating the blue shifted transitions, which carry information about the spin of the QD.

being the identity operator] are

$$
\begin{aligned}
|\alpha\rangle &= \frac{1}{\sqrt{2}}\left[|1\rangle - |4\rangle\right], \\
|\beta\rangle &= \frac{1}{\sqrt{2}}\left[|1\rangle + |4\rangle\right], \\
|\delta\rangle &= \frac{\Omega_c}{A}\left[|2\rangle + \frac{\Delta_1 - \Omega_R}{\Omega_c}|3\rangle\right], \\
|\gamma\rangle &= \frac{\Omega_c}{B}\left[|2\rangle + \frac{\Delta_1 + \Omega_R}{\Omega_c}|3\rangle\right].
\end{aligned}
\tag{21}
$$

In writing Eq. (21) the following magnitudes have been defined:

$$
\begin{aligned}
\Delta_1 &= \Delta_g + \Delta_e, \\
A &= \sqrt{|\Omega_c|^2 + |\Delta_1 - \Omega_R|^2}, \\
B &= \sqrt{|\Omega_c|^2 + |\Delta_1 + \Omega_R|^2}.
\end{aligned}
\tag{22}
$$

The eigenstates in Eq. (21) define a rotation matrix T that diagonalizes the Hamiltonian of Eq. (19) via the matrix product THT^{-1}. Thus the density operator in the dressed basis ρ^D will be given by $\rho^D = T\rho T^{-1}$, ρ being the density matrix operator in the bare basis. Projection of the master equation over the dressed state basis give rise to complicated couplings between the dressed-state populations and coherences. However, the situation can be simplified in the high field limit where the effective Rabi frequency is much greater than all relaxation rates, i.e., $\Omega_R \gg \gamma_{kl}^p$ ($k = 3,4, l = 1,2$). In this case, we can ignore the nonsecular terms, i.e., coupling between population and coherences, since matrix elements associated with various frequencies may be omitted to order $\mathbf{O}(\gamma_{kl}^p/\Omega_R)$. The Bloch equations and the RFS in this basis and in the secular approximation are given in Appendix C.

We present in Fig. 6(a) the eigenvalues given in Eq. (20) as a function of the Rabi frequency Ω_c^0. Note that the energies of the states $|\delta\rangle$ and $|\gamma\rangle$ depend weakly on Ω_c^0. Figure 6(b) displays two adjacent manifolds of states with $N+1$ and N photons. The blue-shifted dressed-state transitions leading to the transition, which preserve the information about the spin of the QD are indicated with solid arrows. The RFS can be shown to be given as a sum of different Lorentzians. The amplitude, center and width of each one of the Lorentzians are provided in Appendix C. In particular, the center of each Lorentzian is determined by computing the difference in energy between the transitions from the manifold of states with $N+1$ photons, $|v_i\rangle \otimes |N+1\rangle$, to the manifold with N photons $|v_j\rangle \otimes |N\rangle$, $|v_i\rangle, |v_j\rangle$ being any of the possible dressed states in Eq. (21).

Now we resort to analyze a representative case of the RFS, as the one with solid line depicted in Fig. 3(b). The spectral features of the RFS arise from the possible transitions between two adjacent manifolds of the Hilbert space [see Fig. 6(b)]. The innermost weak right sideband is attributed to transition $|\beta\rangle \leftrightarrow |\gamma\rangle$ with amplitude $A_{\beta\gamma+}$. In Fig. 6(b) the transitions which carry information about the spin of the QD are indicated, according to the dressed states obtained in Eq. (21). The two highest sidebands on the right side of frequencies ($A_{\delta\alpha+}$ and $A_{\beta\delta+}$), can be attributed to transitions $|\delta\rangle \leftrightarrow |\alpha\rangle$ and $|\delta\rangle \leftrightarrow |\beta\rangle$. The outermost weak right sideband arises from transition $|\delta\rangle \leftrightarrow |\gamma\rangle$ with amplitude $A_{\delta\gamma+}$. Finally the two sidebands enclosed between the two right highest sidebands can be ascribed to transitions $|\alpha\rangle \leftrightarrow |\beta\rangle$ ($A_{\alpha\beta+}$) and $|\alpha\rangle \leftrightarrow |\gamma\rangle$ ($A_{\alpha\gamma+}$), respectively. Numerical simulations carried out reveals that the RFS computed in the dressed picture reproduces the RFS in the bare basis. In view of the previous considerations, we can ascribe the transitions labeled as $S_{\pm x}$ in Fig. 3(b) as the ones produced from dressed state transitions $|\alpha\rangle \leftrightarrow |\beta\rangle$, while the transitions labeled as $S_{\pm y}$ in Fig. 3(b) as the ones produced from dressed-state transitions $|\delta\rangle \leftrightarrow |\gamma\rangle$. It can be easily derived from Eq. (21) that these transitions are only contributed by transitions $|1\rangle \leftrightarrow |4\rangle$ and $|2\rangle \leftrightarrow |3\rangle$, respectively, and they are the unique dressed state transitions, which carry information about the spin of the QD, while the other transitions result in mixing the spin of the QD states.

The spectra computed in the dressed state picture of the isolated QD and the hybrid system are depicted in Fig. 7(a).

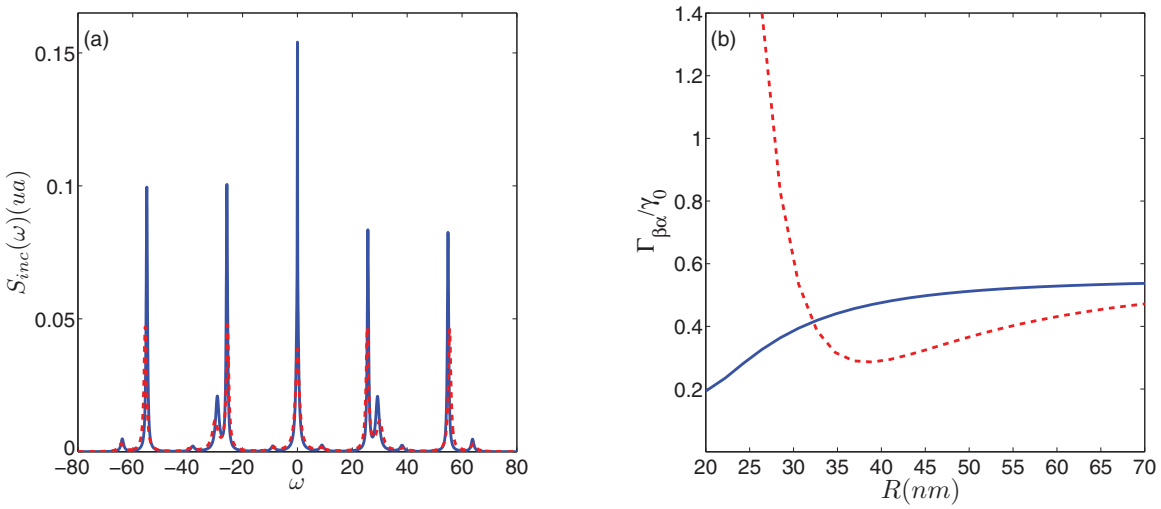

FIG. 7. (Color online) (a) $S_{\rm inc}(\omega)$ versus ω for the isolated QD (dashed line) and the hybrid system (solid line) with $R = 40$ nm, and $\Omega_c^0 = 15\gamma_0$, as in Fig. 3(b). (b) Width of transition $|\alpha\rangle \leftrightarrow |\beta\rangle$ as a function of distance R for different values of the aspect ratio: $q = 2.726$ (solid line) and $q = 4$ (dashed line).

We can devise that the RFS reproduces the results obtained in the bare basis presented in Fig. 3(b), which confirms the validity of the secular approximation in the current situation. The enhancement of the signal labeled as S_{x+} due to the presence of the MNP obtained in Fig. 3(b), can be easily explained in the dressed picture as follows: the maximum value of S_{x+} can be estimated as the peak value of the corresponding Lorentzian associated to transition $|\alpha\rangle \leftrightarrow |\beta\rangle$: $A_{\alpha\beta+}/\Gamma_{\alpha\beta}^2 = \frac{(\rho_{\alpha\alpha})_s}{3+2\gamma_{42}^p/\gamma_{41}^p}$ [see Eqs. (C11) and (C12) in Appendix C]. The steady-state population of the level $|\alpha\rangle$ can be shown to be nearly independent on distance R [in this case $(\rho_{\alpha\alpha})_s \approx 0.06$], thus the enhancement of the peak value of this signal is fully attributable to the plasmon-induced changes of the decay rates. Numerical analysis reveals that the peak value predicted by the dressed-state formulas, which is about 0.019 for $R = 40$ nm, accounts for the enhancement found in the bare state (0.021). In addition, the center of the Lorentzian found at $\omega_{x+} = 29.18$ is also well estimated with the dressed theory at $\omega_{x+} = 29.19$ for $R = 40$ nm. The same predictions also hold in the dressed picture for the other sideband S_{y+} found in Fig. 3(b). Finally, it is worth mentioning that the narrowing of the central line in Fig. 3(b) is also explained in terms of the narrowing of the component $S_0(\omega)$ defined in Appendix C. In addition, the narrowing of the individual components found in the figures of previous section can be explained when considering the dependence of the width of the corresponding Lorentzians on the distance R. To this end we have plotted in Fig. 7(b) the values of the decay rates of the sideband $S_{\pm x}$ ($\Gamma_{\alpha\beta}$) versus the distance R and two values of the aspect ratio q, while keeping fixed the value of the driving field $\Omega_c^0 = 14\gamma_0$. This figure allows us to explain the origin of subnatural linewidths of these sidebands previously observed.

V. CONCLUSIONS

In this work we present a description of the influence of exciton-plasmon interaction in a QD-MNP hybrid system on the RFS. This system has been proposed as a candidate for obtaining high-fidelity spin preparation.[34] The QD is modeled as a four-level-like atomic system and the MNP is considered to be a nanospheroid. We analyze how localized surface charge oscillations in the MNP modify the decay rates of the QD depending on the aspect ratio of the MNP and the distance between the QD and MNP R. Based on the fact that the frequencies of the SPPs are very different along the two principal axes, the decay rate of the atomic transitions parallel to the MNP's major axis would be much different than those parallel to the corresponding minor axis. We show that the anisotropic modification of the decay rates results in modifications of the RFS of the hybrid system. We have predicted that the lines of the RFS can be broadened or narrowed depending on the aspect ratio q, the distance R and the Rabi frequency of the driving field. The modifications of the RFS predicted in this work represents a way for testing experimentally how the exciton-plasmon interaction modifies the properties of the spontaneous emission of the decay pathways in a positively charged QD.

Finally, it should be stated that, although speculative, the hybrid system here investigated can be implemented in realistic QD-MNP systems. Recently, hybrid structures consisting of self-assembled QDs have been grown and covered with metal nanocrystals.[56] In addition, we would like to draw attention to very recent works where the controlled coupling of a single epitaxial QD to a plasmonic nanoantenna has been demonstrated.[57,58] Thus, the structure modeled here could be fabricated using available nanotechnologies for the growth and the precise positioning of the involved elements.

ACKNOWLEDGMENTS

This work has been supported by Spain's Ministerio de Ciencia e Innovación (MCINN) Project No. FIS2010-22082.

APPENDIX A: TOTAL FIELD FELT BY THE QD IN THE PRESENCE OF THE MNP

The electric field appearing in Eq. (5) reads

$$E_{QD}^{(x)} = \frac{1}{\epsilon_{\text{effs}}}\left[E_c + \frac{1}{4\pi\epsilon_0\epsilon_B}\frac{S_x P_{\text{MNP}}^{(x)}}{R^3}\right], \tag{A1}$$

where $\epsilon_{\text{effs}} = (2\epsilon_B + \epsilon_s)/(3\epsilon_B)$, and $S_x = -1$ since the electric field $E_{QD}^{(x)}$ is polarized along the X axis of the hybrid system [see Fig. 1(b)]. The dipole moment $P_{\text{MNP}}^{(x)}$ arises from the charge induced on the surface of the MNP, and depends on the total field due to the QD as[59]

$$P_{\text{MNP}}^{(x)} = 4\pi\epsilon_0\epsilon_B q L_x^3 \gamma_x(\omega_L) E_{\text{MNP}}^{(x)}, \tag{A2}$$

where $E_{\text{MNP}}^{(x)}$ is the slowly varying field amplitude at frequency ω_L felt by the MNP, which is given by

$$E_{\text{MNP}}^{(x)} = E_c + \frac{1}{4\pi\epsilon_0\epsilon_B}\frac{S_x P_{QD}^{(x)}}{R^3}. \tag{A3}$$

In Eq. (A2) the factor $\gamma_x(\omega_L)$ stands for the polarization of the MNP, which reads as

$$\gamma_l(\omega_L) = \frac{\epsilon_m(\omega_L) - \epsilon_B}{3\epsilon_B + 3\varsigma_l(\epsilon_m(\omega_L) - \epsilon_B)}, \quad l = x,y,z, \tag{A4}$$

where ς_l is called the depolarization factor of the MNP,[60] and for a nanospheroid reduces to

$$\begin{aligned}
\varsigma_x &= \frac{1-\varsigma_y}{2},\\
\varsigma_z &= \frac{1-\varsigma_y}{2},\\
\varsigma_y &= \frac{1}{q^2-1}\left[\frac{1}{\sqrt{1-1/q^2}}\log\left(\frac{1+\sqrt{1-1/q^2}}{1-\sqrt{1-1/q^2}}\right) - 1\right].
\end{aligned} \tag{A5}$$

The dipole $P_{QD}^{(x)}$ is expressed via the off-diagonal elements of the density matrix as follows:

$$P_{QD}^{(x)} = \mu_{41}\rho_{41} + \mu_{32}\rho_{32}. \tag{A6}$$

In Eq. (A3) we have not included the factor ϵ_{effs} to account for the screening of the QD dipole field due to the QD dielectric response, since the polarization $P_{QD}^{(x)}$ already contains this factor, as pointed out by Malyshev *et al.*[61] Substituting Eqs. (A3) and (A6) back into Eq. (A2) we obtain

$$\begin{aligned}
P_{\text{MNP}}^{(x)} = {} & 4\pi\epsilon_0\epsilon_B q L_x^3 \gamma_x(\omega_L)\\
& \times\left(E_c + \frac{S_x}{4\pi\epsilon_0\epsilon_B}\frac{\mu_{41}\rho_{41} + \mu_{32}\rho_{32}}{R^3}\right).
\end{aligned}$$

Finally, the slowly varying amplitude of the field in the QD is

$$\begin{aligned}
E_{QD}^{(x)} = {} & \frac{E_c}{\epsilon_{\text{effs}}}\left(1 + \frac{S_x q L_x^3 \gamma_x(\omega_L)}{R^3}\right)\\
& + \frac{q L_x^3 \gamma_x(\omega_L) S_x^2 (\mu_{41}\rho_{41} + \mu_{32}\rho_{32})}{4\pi\epsilon_0\epsilon_B\epsilon_{\text{effs}} R^6}.
\end{aligned} \tag{A7}$$

The result (A7) is plugged into Eq. (5) and we arrive to the result stated in Eq. (6).

APPENDIX B: RESONACE FLUORESCENCE SPECTRUM IN THE BARE-STATE BASIS

The evaluation of the two-time correlation functions that appear in Eq. (15) can be recast to

$$\begin{aligned}
S_{\text{inc}}(\omega) \propto \Re\Big[\int_0^\infty & \big(\mu_{14}^2\langle\Delta\sigma_{41}(\tau)\Delta\sigma_{14}(0)\rangle\\
& + \vec{\mu}_{14}\cdot\vec{\mu}_{23}\langle\Delta\sigma_{41}(\tau)\Delta\sigma_{23}(0)\rangle\\
& + \mu_{24}^2\langle\Delta\sigma_{42}(\tau)\Delta\sigma_{24}(0)\rangle\\
& + \vec{\mu}_{24}\cdot\vec{\mu}_{13}\langle\Delta\sigma_{42}(\tau)\Delta\sigma_{13}(0)\rangle\\
& + \vec{\mu}_{13}\cdot\vec{\mu}_{24}\langle\Delta\sigma_{31}(\tau)\Delta\sigma_{24}(0)\rangle\\
& + \mu_{13}^2\langle\Delta\sigma_{31}(\tau)\Delta\sigma_{13}(0)\rangle\\
& + \vec{\mu}_{23}\cdot\vec{\mu}_{14}\langle\Delta\sigma_{32}(\tau)\Delta\sigma_{14}(0)\rangle\\
& + \mu_{23}^2\langle\Delta\sigma_{32}(\tau)\Delta\sigma_{23}(0)\rangle\big)\, e^{-i\omega\tau} d\tau\Big].
\end{aligned} \tag{B1}$$

The two-time correlation functions can be carried out with the aid of the quantum regression theorem[49,50] and the optical Bloch equations (12). To this end we define the column vector

$$\begin{aligned}
\hat{U}_{jk}(\tau) = {} & [\Delta\sigma_{41}(\tau)\Delta\sigma_{jk}(0), \Delta\sigma_{14}(\tau)\Delta\sigma_{jk}(0),\\
& \Delta\sigma_{42}(\tau)\Delta\sigma_{jk}(0), \Delta\sigma_{24}(\tau)\Delta\sigma_{jk}(0),\\
& \Delta\sigma_{31}(\tau)\Delta\sigma_{jk}(0), \Delta\sigma_{13}(\tau)\Delta\sigma_{jk}(0),\\
& \Delta\sigma_{32}(\tau)\Delta\sigma_{jk}(0), \Delta\sigma_{23}(\tau)\Delta\sigma_{jk}(0),\\
& \Delta\sigma_{21}(\tau)\Delta\sigma_{jk}(0), \Delta\sigma_{12}(\tau)\Delta\sigma_{jk}(0),\\
& \Delta\sigma_{43}(\tau)\Delta\sigma_{jk}(0), \Delta\sigma_{34}(\tau)\Delta\sigma_{jk}(0),\\
& \Delta\sigma_{44}(\tau)\Delta\sigma_{jk}(0), \Delta\sigma_{33}(\tau)\Delta\sigma_{jk}(0),\\
& \Delta\sigma_{22}(\tau)\Delta\sigma_{jk}(0)]^T \; k = 3,4, \quad \text{and}\\
& j = 1,2,
\end{aligned} \tag{B2}$$

where the superindex T stands for transpose. According to the quantum regression theorem, for $\tau > 0$ the vector $\hat{U}_{jk}$ satisfies

$$\frac{d\,\hat{U}_{jk}(\tau)}{d\tau} = M\hat{U}_{jk}(\tau), \tag{B3}$$

M being the 15×15 matrix of the coefficients of Eq. (12).

By working in the Laplace space we obtain the steady-state fluorescence spectrum. Specifically we have

$$\begin{aligned}
S_{\text{inc}}(\omega) \propto \Re\Bigg\{ & \sum_{l=1}^{l=15}[\gamma_{41}R_{1l}(iz) + \sqrt{\gamma_{41}\gamma_{32}}R_{7l}(iz)]\hat{U}_{14}^{(l)}(\infty)\\
& + \sum_{l=1}^{l=15}[\gamma_{42}R_{3l}(iz) + \sqrt{\gamma_{42}\gamma_{31}}R_{5l}(iz)]\hat{U}_{24}^{(l)}(\infty)\\
& + \sum_{l=1}^{l=15}[\gamma_{32}R_{7l}(iz) + \sqrt{\gamma_{41}\gamma_{32}}R_{1l}(iz)]\hat{U}_{23}^{(l)}(\infty)\\
& + \sum_{l=1}^{l=15}[\gamma_{31}R_{5l}(iz) + \sqrt{\gamma_{42}\gamma_{31}}R_{3l}(iz)]\hat{U}_{13}^{(l)}(\infty)\Bigg\},
\end{aligned} \tag{B4}$$

where $\hat{U}_{jk}^{(l)}(\infty)$ is the steady-state value of the lth component of the vector $\hat{U}_{jk}(\tau)$. $R_{jk}(iz)$ is the (j,k) element of the matrix

$R(iz)$ defined as

$$R(iz) = (iz\hat{I} - M)^{-1}, \tag{B5}$$

$\hat{I}$ being the identity matrix with size 15×15, and $z \equiv (\omega - \omega_L)/\gamma_0$.

APPENDIX C: BLOCH EQUATIONS AND RFS IN THE DRESSED-STATE PICTURE

The Bloch equations are given by:

$$\frac{\partial \rho_{\alpha\alpha}}{\partial t} = -\Gamma^{\alpha}_{\alpha\alpha}\rho_{\alpha\alpha} - \Gamma^{\beta}_{\alpha\alpha}\rho_{\beta\beta} - \Gamma^{\delta}_{\alpha\alpha}\rho_{\delta\delta} + \Gamma^{0}_{\alpha\alpha}, \tag{C1}$$

$$\frac{\partial \rho_{\beta\beta}}{\partial t} = -\Gamma^{\alpha}_{\beta\beta}\rho_{\alpha\alpha} - \Gamma^{\beta}_{\beta\beta}\rho_{\beta\beta} - \Gamma^{\delta}_{\beta\beta}\rho_{\delta\delta} + \Gamma^{0}_{\beta\beta}, \tag{C2}$$

$$\frac{\partial \rho_{\delta\delta}}{\partial t} = -\Gamma^{\alpha}_{\delta\delta}\rho_{\alpha\alpha} - \Gamma^{\beta}_{\delta\delta}\rho_{\beta\beta} - \Gamma^{\delta}_{\delta\delta}\rho_{\delta\delta} + \Gamma^{0}_{\delta\delta}, \tag{C3}$$

$$\frac{\partial \rho_{\alpha\beta}}{\partial t} = -[i2\Omega_c + \Gamma_{\alpha\beta}]\rho_{\alpha\beta}, \tag{C4}$$

$$\frac{\partial \rho_{\alpha\delta}}{\partial t} = -[i(\Omega_c - \overline{\Delta} - \Omega_R) + \Gamma_{\alpha\delta}]\rho_{\alpha\delta}, \tag{C5}$$

$$\frac{\partial \rho_{\alpha\gamma}}{\partial t} = -[i(\Omega_c - \overline{\Delta} + \Omega_R) + \Gamma_{\alpha\gamma}]\rho_{\alpha\gamma}, \tag{C6}$$

$$\frac{\partial \rho_{\beta\delta}}{\partial t} = -[-i(\Omega_c + \overline{\Delta} + \Omega_R) + \Gamma_{\beta\delta}]\rho_{\beta\delta}, \tag{C7}$$

$$\frac{\partial \rho_{\beta\gamma}}{\partial t} = -[-i(\Omega_c + \overline{\Delta} - \Omega_R) + \Gamma_{\beta\gamma}]\rho_{\beta\gamma}, \tag{C8}$$

$$\frac{\partial \rho_{\delta\gamma}}{\partial t} = -[i2\Omega_R + \Gamma_{\delta\gamma}]\rho_{\delta\gamma}, \tag{C9}$$

where the decay rates appearing in Eqs. (C1)–(C9) are explicitly given by:

$$\begin{aligned}
\Gamma^{\alpha}_{\alpha\alpha} &= \Gamma^{\beta}_{\beta\beta} = \frac{\gamma^p_{41}}{4} + \frac{\gamma^p_{42}}{2} + \frac{\gamma^p_{31}(\Delta_1 + \Omega_R)^2 + \gamma_{21}|\Omega_c|^2}{2B^2}, \\
\Gamma^{\beta}_{\alpha\alpha} &= \Gamma^{\alpha}_{\beta\beta} = -\frac{\gamma^p_{41}}{4} + \frac{\gamma^p_{31}(\Delta_1 + \Omega_R)^2 + \gamma_{21}|\Omega_c|^2}{2B^2}, \\
\Gamma^{\delta}_{\alpha\alpha} &= \Gamma^{\delta}_{\beta\beta} = -\frac{\gamma^p_{31}(\Delta_1 - \Omega_R)^2 + \gamma_{21}|\Omega_c|^2}{2A^2} \\
&\quad + \frac{\gamma^p_{31}(\Delta_1 + \Omega_R)^2 + \gamma_{21}|\Omega_c|^2}{2B^2}, \\
\Gamma^{0}_{\alpha\alpha} &= \Gamma^{0}_{\beta\beta} = \frac{\gamma^p_{31}(\Delta_1 + \Omega_R)^2 + \gamma_{21}|\Omega_c|^2}{2B^2}, \\
\Gamma^{\alpha}_{\delta\delta} &= \Gamma^{\beta}_{\delta\delta} = -\frac{\gamma^p_{42}|\Omega_c|^2}{2A^2} + \frac{\gamma^p_{32}|\Omega_c|^2(\Delta_1 + \Omega_R)^2}{A^2B^2}, \\
\Gamma^{\delta}_{\delta\delta} &= \frac{(\gamma^p_{31} + \gamma^p_{32})(\Delta_1 - \Omega_R)^2 + \gamma_{21}|\Omega_c|^2}{A^2} \\
&\quad - \frac{\gamma^p_{32}|\Omega_c|^2(\Delta_1 - \Omega_R)^2}{A^4} + \frac{\gamma^p_{32}|\Omega_c|^2(\Delta_1 + \Omega_R)^2}{A^2B^2}, \\
\Gamma^{0}_{\delta\delta} &= \frac{\gamma^p_{32}|\Omega_c|^2(\Delta_1 + \Omega_R)^2}{A^2B^2}. \\
\Gamma_{\alpha\beta} &= \frac{3}{4}\gamma^p_{41} + \frac{\gamma^p_{42}}{2}, \\
\Gamma_{\alpha\delta} &= \Gamma_{\beta\delta} = \frac{\gamma^p_{41} + \gamma^p_{42}}{4} \\
&\quad + \frac{(\gamma^p_{31} + \gamma^p_{32})(\Delta_1 - \Omega_R)^2 + \gamma_{21}|\Omega_c|^2}{2A^2}, \\
\Gamma_{\alpha\gamma} &= \Gamma_{\beta\gamma} = \frac{\gamma^p_{41} + \gamma^p_{42}}{4} \\
&\quad + \frac{(\gamma^p_{31} + \gamma^p_{32})(\Delta_1 + \Omega_R)^2 + \gamma_{21}|\Omega_c|^2}{2B^2}, \\
\Gamma_{\delta\gamma} &= \frac{(\gamma^p_{31} + \gamma^p_{32})(\Delta_1 + \Omega_R)^2 + \gamma_{21}|\Omega_c|^2}{2B^2} \\
&\quad + \frac{(\gamma^p_{31} + \gamma^p_{32})(\Delta_1 - \Omega_R)^2 + \gamma_{21}|\Omega_c|^2}{2A^2} \\
&\quad - \frac{\gamma^p_{32}|\Omega_c|^2(\Delta_1^2 - \Omega_R^2)}{A^2B^2}.
\end{aligned} \tag{C10}$$

The RFS is obtained in the dressed-state basis by applying the quantum regression theorem to the dressed equations (C1)–(C9). After a lengthy but straightforward calculation, the RFS in this basis $[S_{\mathrm{inc,DS}}(\omega)]$ can be shown to be given by:

$$\begin{aligned}
S_{\mathrm{inc,DS}}(\omega) \propto \Re\Bigg[& \frac{A_{\alpha\beta-}}{\Gamma_{\alpha\beta} + i(2\Omega_c + \omega)} + \frac{A_{\alpha\beta+}}{\Gamma_{\alpha\beta} - i(2\Omega_c - \omega)} + \frac{A_{\alpha\delta+}}{\Gamma_{\alpha\delta} + i(\Omega_c - \bar{\Delta} - \Omega_R + \omega)} + \frac{A_{\alpha\delta-}}{\Gamma_{\alpha\delta} - i(\Omega_c - \bar{\Delta} - \Omega_R - \omega)} \\
& + \frac{A_{\alpha\gamma-}}{\Gamma_{\alpha\gamma} + i(\Omega_c - \bar{\Delta} + \Omega_R + \omega)} + \frac{A_{\alpha\gamma+}}{\Gamma_{\alpha\gamma} - i(\Omega_c - \bar{\Delta} + \Omega_R - \omega)} + \frac{A_{\beta\gamma+}}{\Gamma_{\beta\gamma} - i(\Omega_c + \bar{\Delta} - \Omega_R - \omega)} \\
& + \frac{A_{\beta\gamma-}}{\Gamma_{\beta\gamma} + i(\Omega_c + \bar{\Delta} - \Omega_R + \omega)} + \frac{A_{\beta\delta+}}{\Gamma_{\beta\delta} - i(\Omega_c + \bar{\Delta} + \Omega_R - \omega)} + \frac{A_{\beta\delta-}}{\Gamma_{\beta\delta} + i(\Omega_c + \bar{\Delta} + \Omega_R + \omega)} \\
& + \frac{A_{\delta\gamma-}}{\Gamma_{\delta\gamma} + i(2\Omega_R + \omega)} + \frac{A_{\delta\gamma+}}{\Gamma_{\delta\gamma} - i(2\Omega_R - \omega)} + S_0(\omega)\Bigg].
\end{aligned} \tag{C11}$$

A close inspection of Eq. (C11) reveals that the RFS can be decomposed as a sum of Lorentzian functions with different amplitude coefficients $[A_{jk\pm}\,(j,k = \alpha,\beta,\gamma,\delta)]$, and located at specific positions: the plus/minus sign is used for the blue/red sidebands. The center of each Lorentzian is determined by computing the difference in energy between the transitions from the manifold of states with N photons, $|v_i\rangle \otimes |N\rangle$, to the manifold with $N-1$ photons $|v_j\rangle \otimes |N-1\rangle$, $|v_i\rangle, |v_j\rangle$ being

any of the possible dressed states in Eq. (21). The expressions for the coefficients A_i in Eq. (C11) read:

$$
\begin{aligned}
A_{\alpha\beta+} &= \frac{\gamma_{41}^{p}(\rho_{\alpha\alpha})_s}{4},\\
A_{\alpha\beta-} &= \frac{\gamma_{41}^{p}(\rho_{\beta\beta})_s}{4},\\
A_{\alpha\delta+} &= \frac{\gamma_{31}^{p}A^2(\rho_{\delta\delta})_s}{8\Omega_R^2},\\
A_{\alpha\delta-} &= \frac{\gamma_{42}^{p}A^2(\Delta_1+\Omega_R)^2(\rho_{\alpha\alpha})_s}{8\Omega_R^2\Omega_c^2},\\
A_{\alpha\gamma+} &= \frac{\gamma_{31}^{p}B^2(\rho_{\gamma\gamma})_s}{8\Omega_R^2},\\
A_{\alpha\gamma-} &= \frac{\gamma_{42}^{p}B^2(\Delta_1-\Omega_R)^2(\rho_{\alpha\alpha})_s}{8\Omega_R^2\Omega_c^2},\\
A_{\beta\gamma+} &= A_{\alpha\gamma+},\\
A_{\beta\gamma-} &= \frac{\gamma_{42}^{p}B^2(\Delta_1-\Omega_R)^2(\rho_{\beta\beta})_s}{8\Omega_R^2\Omega_c^2},\\
A_{\beta\delta+} &= A_{\alpha\delta+},\\
A_{\beta\delta-} &= \frac{\gamma_{42}^{p}A^2(\Delta_1+\Omega_R)^2(\rho_{\beta\beta})_s}{8\Omega_R^2\Omega_c^2},\\
A_{\delta\gamma+} &= \frac{\gamma_{32}^{p}A^2B^2(\Delta_1-\Omega_R)^2(\rho_{\delta\delta})_s}{16\Omega_R^4\Omega_c^2},\\
A_{\delta\gamma-} &= \frac{\gamma_{32}^{p}A^2B^2(\Delta_1+\Omega_R)^2(\rho_{\gamma\gamma})_s}{16\Omega_R^4\Omega_c^2},
\end{aligned}
\tag{C12a}
$$

and $S_0(\omega)$ stands for the central peak of the incoherent resonance spectrum. The terms $(\rho_{ii})_s$ $(i=\alpha,\ \beta,\ \delta,\ \gamma)$ stand for the steady-state populations of the dressed states, while $\bar{\Delta}$, A and B are given in Eq. (22).

To evaluate $S_0(\omega)$ appearing in Eq. (C11), let us define the vector of populations in the steady-state:

$$
(\hat{\rho})_s = [(\rho_{\alpha\alpha})_s,(\rho_{\beta\beta})_s,(\rho_{\delta\delta})_s]^T, \tag{C13}
$$

where superscript T stands for transpose. The components of vector $(\hat{\rho})_s$ satisfy the following equation:

$$
B\cdot(\hat{\rho})_s = \hat{\Gamma}^0,
$$

where B is the matrix of coefficients from equations (C1)–(C3) and $\hat{\Gamma}^0$ is a column vector whose jth component is $-\Gamma^0_{jj}$, $j=\alpha,\beta,\delta$, defined in Eq. (C11).

The central peak of the incoherent resonance spectrum is given by:

$$
\begin{aligned}
S_0(\omega) \propto \Re\Bigg\{\int_0^\infty \Bigg[&\frac{\gamma_{41}}{2}(\langle\Delta\sigma_{\alpha\alpha}(\tau)\Delta\sigma_{\alpha\alpha}(0)\rangle + \langle\Delta\sigma_{\beta\beta}(\tau)\Delta\sigma_{\alpha\alpha}(0)\rangle - \langle\Delta\sigma_{\alpha\alpha}(\tau)\Delta\sigma_{\beta\beta}(0)\rangle + \langle\Delta\sigma_{\beta\beta}(\tau)\Delta\sigma_{\beta\beta}(0)\rangle)\\
&+\frac{\sqrt{\gamma_{41}\gamma_{32}}}{8\Omega_R^2\Omega_c}(A^2(\Delta_1+\Omega_R)\langle\Delta\sigma_{\delta\delta}(\tau)\Delta\sigma_{\alpha\alpha}(0)\rangle + B^2(\Delta_1-\Omega_R)\langle\Delta\sigma_{\gamma\gamma}(\tau)\Delta\sigma_{\alpha\alpha}(0)\rangle\\
&-A^2(\Delta_1+\Omega_R)\langle\Delta\sigma_{\delta\delta}(\tau)\Delta\sigma_{\beta\beta}(0)\rangle - B^2(\Delta_1-\Omega_R)\langle\Delta\sigma_{\gamma\gamma}(\tau)\Delta\sigma_{\beta\beta}(0)\rangle\\
&+A^2(\Delta_1+\Omega_R)\langle\Delta\sigma_{\alpha\alpha}(\tau)\Delta\sigma_{\delta\delta}(0)\rangle - A^2(\Delta_1+\Omega_R)\langle\Delta\sigma_{\beta\beta}(\tau)\Delta\sigma_{\delta\delta}(0)\rangle\\
&+B^2(\Delta_1-\Omega_R)\langle\Delta\sigma_{\alpha\alpha}(\tau)\Delta\sigma_{\gamma\gamma}(0)\rangle - B^2(\Delta_1-\Omega_R)\langle\Delta\sigma_{\beta\beta}(\tau)\Delta\sigma_{\gamma\gamma}(0)\rangle)\\
&+\frac{\gamma_{32}}{16\Omega_R^4\Omega_c^2}(A^4(\Delta_1+\Omega_R)^2\langle\Delta\sigma_{\delta\delta}(\tau)\Delta\sigma_{\delta\delta}(0)\rangle + A^2B^2\left(\Delta_1^2-\Omega_R^2\right)\langle\Delta\sigma_{\gamma\gamma}(\tau)\Delta\sigma_{\delta\delta}(0)\rangle\\
&+A^2B^2\left(\Delta_1^2-\Omega_R^2\right)\langle\Delta\sigma_{\delta\delta}(\tau)\Delta\sigma_{\gamma\gamma}(0)\rangle + B^4(\Delta_1-\Omega_R)^2\langle\Delta\sigma_{\gamma\gamma}(\tau)\Delta\sigma_{\gamma\gamma}(0)\rangle)\Bigg]e^{-i\omega\tau}d\tau\Bigg\},
\end{aligned}
\tag{C14}
$$

where $\Delta\sigma_{jj}(\tau)=\sigma_{jj}(\tau)-\langle\sigma_{jj}(\infty)\rangle$, $j=\alpha,\ \beta,\ \delta,\ \gamma$, stand for the deviation from the steady state of the operators $\sigma_{jj}=|j\rangle\langle j|$. The two-time correlation functions from Eq. (C14) can be computed by invoking the quantum regression theorem together with the Eqs. (C1)–(C3). We define the column vector:

$$
\begin{aligned}
\hat{U}^j(\tau) = [&\langle\Delta\sigma_{\alpha\alpha}(\tau)\Delta\sigma_{jj}(0)\rangle,\quad \langle\Delta\sigma_{\beta\beta}(\tau)\Delta\sigma_{jj}(0)\rangle,\\
&\langle\Delta\sigma_{\delta\delta}(\tau)\Delta\sigma_{jj}(0)\rangle]^T.
\end{aligned}
\tag{C15}
$$

According to the quantum regression theorem, for $\tau>0$ the vector $\hat{U}^j(\tau)$ satisfies the equation

$$
\frac{\partial\hat{U}^j(\tau)}{\partial\tau} = B\cdot\hat{U}^j(\tau)(j=\alpha,\beta,\delta,\gamma), \tag{C16}
$$

B being the matrix of coefficients from equations (C1)–(C3) (note that $\langle\sigma_{ij}\rangle=\rho_{ji}$). Working with Eq. (C16) in the Laplace space, we obtain the values for the two-time correlation functions from Eq. (C14):

$$
\int_0^\infty\langle\Delta\sigma_{\alpha\alpha}(\tau)\Delta\sigma_{jj}(0)\rangle e^{-i\omega\tau} = \sum_{m=1}^{3}R_{1m}(iz)\cdot\left(\hat{U}_m^j\right)_s, \tag{C17}
$$

$$
\int_0^\infty\langle\Delta\sigma_{\beta\beta}(\tau)\Delta\sigma_{jj}(0)\rangle e^{-i\omega\tau} = \sum_{m=1}^{3}R_{2m}(iz)\cdot\left(\hat{U}_m^j\right)_s, \tag{C18}
$$

$$
\int_0^\infty\langle\Delta\sigma_{\delta\delta}(\tau)\Delta\sigma_{jj}(0)\rangle e^{-i\omega\tau} = \sum_{m=1}^{3}R_{3m}(iz)\cdot\left(\hat{U}_m^j\right)_s, \tag{C19}
$$

$$
\begin{aligned}
&\int_0^\infty\langle\Delta\sigma_{\gamma\gamma}(\tau)\Delta\sigma_{jj}(0)\rangle e^{-i\omega\tau}\\
&\quad= -\sum_{m=1}^{3}(R_{1m}(iz)+R_{2m}(iz)+R_{3m}(iz))\cdot\left(\hat{U}_m^j\right)_s,
\end{aligned}
\tag{C20}
$$

where we have set $z\equiv(\omega-\omega_L)/\gamma_0$. $(\hat{U}_m^j)_s$ stands for the mth component of the vector $\hat{U}_m^j(\tau)$ evaluated in the steady state

($\tau = \infty$), and $R_{nm}(s)$ is the (n,m) element of the matrix

$$R(iz) = (iz\hat{I} - B)^{-1}, \tag{C21}$$

$\hat{I}$ being the 3×3 identity matrix. Equations (C17)–(C20) can be substituted back into Eq. (C14), which allows for the numerical computation of the central line of the RFS.

[1] P. Michler, A. Imamoglu, M. D. Mason, P. J. Carson, G. F. Strouse, and S. K. Buratto, Nature (London) **406**, 968 (2000).
[2] D. Loss and D. P. DiVincenzo, Phys. Rev. A **57**, 120 (1998).
[3] J. M. Elzerman, R. Hanson, L. H. Willems van Beveren, B. Witkamp, L. M. K. Vandersypen, and L. P. Kouwenhoven, Nature (London) **430**, 431 (2004).
[4] D. Heiss, S. Schaeck, H. Huebl, M. Bichler, G. Abstreiter, J. J. Finley, D. V. Bulaev, and D. Loss, Phys. Rev. B **76**, 241306 (2007).
[5] A. Zrenner E. Beham, S. Stufler, F. Findeis, M. Bichler, and G. Abstreiter, Nature (London) **418**, 612 (2002).
[6] X. Li, Y. Wu, D. Steel, D. Gammon, T. H. Stievater, D. S. Katzer, D. Park, C. Piermarocchi, and L. J. Sham, Science **301**, 809 (2003).
[7] X. Xu, B. Sun, P. R. Berman, D. G. Steel, A. S. Bracker, D. Gammon, and L. J. Sham, Science **317**, 929 (2007).
[8] A. Muller, E. B. Flagg, P. Bianucci, X. Y. Wang, D. G. Deppe, W. Ma, J. Zhang, G. J. Salamo, M. Xiao, and C. K. Shih, Phys. Rev. Lett. **99**, 187402 (2007).
[9] E. B. Flagg, A. Muller, J. W. Robertson, S. Founta, D. G. Deppe, M. Xiao, W. Ma, G. J. Salamo, and C. K. Shih, Nature Phys. **5**, 203 (2009).
[10] A. Muller, W. Fang, J. Lawall, and G. S. Solomon, Phys. Rev. Lett. **101**, 027401 (2008).
[11] X. Xu, B. Sun, E. D. Kim, K. Smirl, P. R. Berman, D. G. Steel, A. S. Bracker, D. Gammon, and L. J. Sham, Phys. Rev. Lett. **101**, 227401 (2008).
[12] X. Xu, B. Sun, P. R. Berman, D. G. Steel, D. Gammon, and L. J. Sham, Solid Stat. Commun. **149**, 1479 (2009).
[13] A. Imamoglu, D. D. Awschalom, G. Burkard, D. P. DiVincenzo, D. Loss, M. Sherwin, and A. Small, Phys. Rev. Lett. **83**, 4204 (1999).
[14] H. J. Kimble and L. Mandel, Phys. Rev. A **13**, 2123 (1976).
[15] A. N. Vamivakas, Y. Zhao1, Chao-Yang Lu, and M. Atatüre, Nature Phys. **5**, 198 (2009).
[16] C. Matthiesen, A. N. Vamivakas, and M. Atatüre, Phys. Rev. Lett. **108**, 093602 (2012).
[17] K. Konthasinghe, J. Walker, M. Peiris, C. K. Shih, Y. Yu, M. F. Li, J. F. He, L. J. Wang, H. Q. Ni, Z. C. Niu, and A. Muller, Phys. Rev. B **85**, 235315 (2012).
[18] E. M. Purcell, H. C. Torrey, and R. V. Pound, Phys. Rev. **69**, 37 (1946).
[19] W. Zhang, A. O. Govorov, and G. W. Bryant, Phys. Rev. Lett. **97**, 146804 (2006).
[20] R. D. Artuso and G. W. Bryant, Nano Lett. **8**, 2106 (2008).
[21] K. T. Shimizu, W. K. Woo, B. R. Fisher, H. J. Eisler, and M. G. Bawendi, Phys. Rev. Lett. **89**, 117401 (2002).
[22] A. O. Govorov, G. W. Bryant, W. Zhang, T. Skeini, J. Lee, N. A. Kotov, J. M. Slocik, and R. R. Naik, Nano Lett. **6**, 984 (2006).
[23] A. Manjavacas, F. J. García de Abajo, and P. Nordlander, Nano Lett. **11**, 2318 (2011).
[24] A. Manjavacas, P. Nordlander, and F. J. García de Abajo, ACS Nano **2**, 1724 (2012).
[25] F. H. L. Koppens, D. E. Chang, and F. J. García de Abajo, Nano Lett. **11**, 3370 (2011).
[26] V. V. Klimov, M. Ducloy, and V. S. Letokhov, Eur. Phys. J. D **20**, 133 (2002).
[27] A. Ridolfo, O. Di Stefano, N. Fina, R. Saija, and S. Savasta, Phys. Rev. Lett. **105**, 263601 (2010).
[28] D. Ratchford, F. Shafiei, S. Kim, S. K. Gray, and X. Li, Nano Lett. **11**, 1049 (2011).
[29] Y. Gu, L. Huang, O. J. F. Martin, and Q. Gong, Phys. Rev. B **81**, 193103 (2010).
[30] Y. V. Vladimirova, V. V. Klimov, V. M. Pastukhov, and V. N. Zadkov, Phys. Rev. A **85**, 053408 (2012).
[31] D. V. Bulaev and D. Loss. Phys. Rev. Lett. **95**, 076805 (2005).
[32] D. Brunner, B. D. Gerardot, P. A. Dalgarno, G. Wüst, K. Karrai, N. G. Stoltz, P. M. Petroff, and R. J. Warburton, Science **325**, 70 (2009).
[33] D. Brunner, Ph.D. thesis, Heriot-Watt University, 2010, http://hdl.handle.net/10399/2350.
[34] M. A. Antón, F. Carreño, Sonia Melle, Oscar G. Calderón, E. Cabrera-Granado, and Mahi R. Singh, Phys. Rev. B **87**, 195303 (2013).
[35] B. D. Gerardot, D. Brunner, P. A. Dalgarno, P. Öhberg, S. Seidl, M. Kroner, K. Karrai, N. G. Stoltz, P. M. Petroff, and R. J. Warburton, Nature (London) **451**, 441 (2008).
[36] X. Xu, Y. Wu, B. Sun, Q. Huang, J. Cheng, D. G. Steel, A. S. Bracker, D. Gammon, C. Emary, and L. J. Sham, Phys. Rev. Lett. **99**, 097401 (2007).
[37] M. Kroner, K. M. Weiss, B. Biedermann, S. Seidl, A. W. Holleitner, A. Badolato, P. M. Petroff, P. Öhberg, R. J. Warburton, and K. Karrai, Phys. Rev. B **78**, 075429 (2008).
[38] E. D. Kim, K. Truex, X. Xu, B. Sun, D. G. Steel, A. S. Bracker, D. Gammon, and L. J. Sham, Phys. Rev. Lett. **104**, 167401 (2010).
[39] D. Press, T. D. Ladd, B. Zhang, and Y. Yamamoto, Nature (London) **456**, 218 (2008).
[40] H. T. Dung, L. Knoll, and D. G. Welsch, Phys. Rev. A **66**, 063810 (2002).
[41] S. M. Sadeghi, Nanotech. **20**, 225401 (2009).
[42] J. Gersten and A. Nitzan, J. Chem. Phys. **75**, 1139 (1981).
[43] L. Novotny, Appl. Phys. Lett. **69**, 3806 (1996).
[44] F. J. García de Abajo and J. Aizpurúa, Phys. Rev. B **56**, 15873 (1997).
[45] L. A. Blanco and F. J. García de Abajo, J. Quant. Spectr. Rad. Trans. **89**, 37 (2004).
[46] R. Carminati, J.-J. Greffet, C. Henkel, and J. M. Vigoureux, Opt. Comm. **261**, 368 (2006).
[47] A. O. Govorov, J. Lee, and N. A. Kotov, Phys. Rev. B **76**, 125308 (2007).
[48] M. A. Antón, F. Carreño, S. Melle, O. G. Calderón, E. Cabrera-Granado, J. Cox, and M. R. Singh, Phys. Rev. B **86**, 155305 (2012).

[49]M. O. Scully and M. S. Zubairy, *Quantum Optics* (Cambridge University Press, London, 1997).
[50]M. Lax, Phys. Rev. **172**, 350 (1968).
[51]P. B. Johnson and R. W. Christy, Phys. Rev. B **6**, 4370 (1972).
[52]D. Kleppner, Phys. Rev. Lett. **47**, 233 (1981).
[53]P. Anger, P. Bharadwaj, and L. Novotny, Phys. Rev. Lett. **96**, 113002 (2006).
[54]M. T. Cheng, S. D. Liu, H. J. Zhou, Z. H. Hao, and Q. Q. Wang, Opt. Lett. **32**, 2125 (2007).
[55]G. Lu, T. Zhang, W. Li, L. Hou, J. Liu, and Q. Gong, J. Phys. Chem. C **115**, 15822 (2011).
[56]A. Urbańczyk, G. J. Hamhuis, and R. Nötzel, Appl. Phys. Lett. **96**, 113101 (2010).
[57]M. Pfeiffer, K. Lindfors, C. Wolpert, P. Atkinson, M. Benyoucef, A. Rastelli, O. G. Schmidt, H. Giessen, and M. Lippitz, Nano Lett. **10**, 4555 (2010).
[58]M. Pfeiffer, K. Lindfors, P. Atkinson3, A. Rastelli, O. G. Schmidt, H. Giessen, and M. Lippitz, Phys. Status Solidi **249**, 678 (2012).
[59]A. O. Govorov, Phys. Rev. B **82**, 155322 (2010).
[60]C. F. Bohren and D. R. Huffman, *Absorption and Scattering of Light by Small Particles* (Wiley, New York, 1983), Chap. 5.
[61]A. V. Malyshev and V. A. Malyshev, Phys. Rev. B **84**, 035314 (2011).